

Three-dimensional mapping of the altermagnetic spin splitting in CrSb

Guowei Yang^{*1}, Zhanghuan Li^{†2}, Sai Yang^{‡3}, Jiyuan Li^{‡3}, Hao Zheng^{‡1}, Weifan Zhu^{‡1}, Ze Pan^{‡1}, Yifu Xu^{‡1}, Saizheng Cao^{‡1}, Wenxuan Zhao^{‡4}, Anupam Jana^{‡5,6}, Jiawen Zhang^{‡1}, Mao Ye^{‡7}, Yu Song^{‡1}, Lun-Hui Hu^{‡1}, Lexian Yang^{‡4}, Jun Fujii^{‡5}, Ivana Vobornik^{‡5}, Ming Shi^{‡1}, Huiqiu Yuan^{‡1,8,9}, Yongjun Zhang^{‡3}, Yuanfeng Xu^{‡§1} and Yang Liu^{‡¶1,8}

¹Center for Correlated Matter and School of Physics, Zhejiang University, Hangzhou 310058, China

²Beijing National Laboratory for Condensed Matter Physics, Institute of Physics, Chinese Academy of Sciences, Beijing 100190, China

³Hubei Key Laboratory of Photoelectric Materials and Devices, School of Materials Science and Engineering, Hubei Normal University, Huangshi 435002, China

⁴State Key Laboratory of Low Dimensional Quantum Physics, Department of Physics, Tsinghua University, Beijing 100084, China

⁵CNR-IOM, TASC Laboratory, Area Science Park-Basovizza, Trieste 34139, Italy

⁶International Center for Theoretical Physics (ICTP), Trieste 34151, Italy

⁷Shanghai Synchrotron Radiation Facility, Shanghai Advanced Research Institute, Chinese Academy of Sciences, Shanghai 201204, China

⁸Collaborative Innovation Center of Advanced Microstructures, Nanjing University, Nanjing 210093, China

⁹State Key Laboratory of Silicon and Advanced Semiconductor Materials, Zhejiang University, Hangzhou 310058, Peoples Republic of China

Abstract

Altermagnetism, a kind of collinear magnetism that is characterized by a momentum-dependent band and spin splitting without net magnetization, has recently attracted considerable interest. Finding altermagnetic materials with large splitting near the Fermi level necessarily requires three-dimensional k -space mapping. While this is crucial for spintronic applications and emergent phenomena, it remains challenging. Here, using synchrotron-based angle-resolved photoemission spectroscopy (ARPES), spin-resolved ARPES and model calculations, we uncover a large altermagnetic splitting, up to ~ 1.0 eV, near the Fermi level in CrSb. We verify its bulk-type g -wave altermagnetism through systematic three-dimensional k -space mapping, which unambiguously reveals the altermagnetic symmetry and associated nodal planes. Spin-resolved ARPES measurements further verify the spin polarizations of the split bands near Fermi level. Tight-binding model analysis indicates that the large altermagnetic splitting arises from strong third-nearest-neighbor hopping mediated by Sb ions. The large band/spin splitting near Fermi level in metallic CrSb, together with its high T_N (up to 705 K) and simple spin configuration, paves the way for exploring emergent phenomena and spintronic applications based on altermagnets.

*These authors contributed equally to this paper

†These authors contributed equally to this paper

‡y.jzhang@hbnu.edu.cn

§y.xu@zju.edu.cn

¶yangliuphys@zju.edu.cn

Introduction

A new type of collinear magnetism, dubbed altermagnetism, has been proposed theoretically [1–11] and verified experimentally in MnTe [12–17]. There have also been experiments supporting altermagnetism in RuO₂ [18–23], although the nature of magnetism in RuO₂ is still debated [24,25]. Altermagnet is often defined in the absence of spin-orbit coupling (SOC) and can be classified by the spin space group, different from ferromagnet and conventional antiferromagnet. Although altermagnets exhibit zero net magnetization in real space, they host spin-split electronic bands in reciprocal space. While the zero bulk magnetization allows for ultrafast manipulation with low stray field, akin to an antiferromagnet, the time-reversal symmetry breaking and momentum-dependent spin polarization in altermagnets can give rise to emergent properties useful for device applications, such as anomalous/nonlinear Hall effects [17–19,26–30], giant/tunneling magnetoresistance [31,32], spin currents, spin-torque effects [20–22,33–36], spin caloritronics (Nernst effect) [37–39]. Recent theoretical studies further show that the inclusion of SOC can induce topological states [40,41]. In addition, unconventional superconductivity based on altermagnetic materials has been theoretically proposed [42–47], making them a fertile playground for exploring superconducting states. The momentum-dependent spin splitting has also been found recently in the noncoplanar system MnTe₂ [48], which significantly expands the scope of altermagnetic materials.

The characteristic momentum-dependent spin splitting in an altermagnet results from its special spin-group symmetry [10,49], i.e., the opposite-spin sublattices are connected by a real-space rotation or mirror operation, instead of a translation or inversion. Depending on the dimensionality and lattice/spin symmetry, altermagnets can be classified into planar-type or bulk-type with d -, g - or i -wave symmetry [9], corresponding to two, four or six spin-degenerate nodal planes crossing the Γ point, respectively. Since the nodal planes often coincide with high-symmetry momentum planes, it is important to investigate the altermagnetic splitting in three-dimensional momentum space. While altermagnetic splittings have been observed experimentally in MnTe, how the altermagnetic splitting evolves in three-dimensional momentum space remains unexplored. Most importantly, for enhanced physical properties and real applications, it is critical to find strong altermagnets with large spin splittings near the Fermi level (E_F) and with magnetic ordering temperature well above room temperature.

Here in this paper, we present direct spectroscopic evidence of the largest altermagnetic band splitting reported so far, up to ~ 1.0 eV near E_F in CrSb, from synchrotron-based angle-resolved photoemission spectroscopy (ARPES) and spin-resolved ARPES measurements, combined with *ab initio* calculations and tight-binding (TB) model analysis. CrSb is traditionally known for its itinerant antiferromagnetism with a high Néel temperature up to 705 K [50]. Although altermagnetic band splitting was recently reported in (100)-oriented CrSb films by soft X-ray ARPES [51], high-resolution three-dimensional k -space mapping of the altermagnetic splitting with spin resolution, which is key to confirm (and understand) the altermagnetism proposed in CrSb [9], is still lacking. Our high-resolution ARPES data from (001)-oriented single crystals unambiguously reveal the characteristic k_z and in-plane momentum dependence of the altermagnetic splitting in CrSb. Moreover, our spin-resolved ARPES measurements provide direct evidence of the expected spin polarization near E_F . The experimental results are in good agreement with the *ab initio* calculations from density functional theory (DFT). We further demonstrate through TB model analysis that the large altermagnetic splitting stems from the strong third-nearest-neighbor hoppings of Cr $3d$ orbitals mediated by the Sb $5p$ orbitals, which break both the space-time reversal symmetry and the translational spin-rotation symmetry. Such insight can be important for designing and tuning altermagnetic materials with desirable properties.

Results

Sample characterization and lattice/spin structure.

CrSb crystallizes in the hexagonal NiAs-type structure. As shown in Fig. 1a, each Cr atom is coordinated to the top and bottom Sb triangles with AB stacking, forming a tilted octahedron. The sharp X-ray diffraction (XRD) pattern from a (001)-oriented crystal, shown in Fig. 1b, confirms the high crystal quality with the extracted lattice constants of $a = b = 4.12 \text{ \AA}$, $c = 5.44 \text{ \AA}$, close to the previously reported value of $a = 4.12 \text{ \AA}$ and $c = 5.47 \text{ \AA}$ [50]. The magnetic structure of CrSb, confirmed by a number of studies based on neutron scattering [50, 52–54], belongs to the magnetic space group $P6'_3/m'm'c$, where the magnetic moments of Cr (aligned along the [001] axis) are parallel within the hexagonal Cr layer and antiparallel between two neighboring layers. Ignoring the SOC, which is weak for Cr 3d electrons and plays a minor role in the low-energy band structure (see below), the altermagnetism in CrSb can be well defined and characterized by non-relativistic spin-group symmetries. As defined in [9, 10, 55–59], a spin space group operation is a combination of spin rotation operation and real-space transformation, namely $[R_i^s || R_j]$, where R_i^s acts only in spin space (containing only identity transformation E and spin-flip operation C_2^s for collinear magnetic systems), while R_j operates in real space. The two opposite-spin sublattices in altermagnets should be connected by a (screw) n -fold rotation ($(C_n, n$ depending on lattice/spin symmetries) or (glide) mirror (M) symmetry in real space, rather than by translation (\vec{t}) or inversion (P) symmetry. As illustrated in Fig. 1c, the two Cr sublattices with opposite spins in CrSb are related by a spin group symmetry $[C_2^s || M_z]$ or $[C_2^s || \tilde{C}_{6z}]$, where \tilde{C}_{6z} is a six-fold rotation along z axis combined with a translation $\vec{t} = (0, 0, \frac{1}{2})c$. Both the spin group symmetries $[C_2^s || \vec{t}]$ and $[T || P]$ (space-time reversal) are broken in CrSb, resulting in momentum-dependent spin splitting in the electronic band structure. As shown in Fig. 1d, on the mirror invariant planes, i.e. the horizontal planes at $k_z = 0$ and $0.5c^*$ ($c^* = 2\pi/c$), and three equivalent vertical planes containing $\bar{K} - \bar{\Gamma} - \bar{K}$ related to C_{3z} , the spin splitting is zero. Therefore, CrSb can be classified as a three-dimensional (or bulk-type) g -wave altermagnet with four nodal planes crossing the Γ point [9].

The in-plane k_x - k_y map from ARPES measurements using 200 eV photons is shown in Fig. 1e, which shows (hole-like) pockets centered at $\bar{\Gamma}$ with the in-plane periodicity consistent with the (001) surface. Based on the standard understanding of photoemission [60, 61], ARPES measurements under different photon energies probe electronic states with different k_z values. The conversion between photon energy and k_z is determined by the inner potential V_0 , which is the difference between the crystal potential and the vacuum level. The k_z dispersion of the valence bands along $\bar{\Gamma} - \bar{M}$, obtained from the photon-energy-dependent scan, is shown in Fig. 1f. The observed periodic modulation of the bands with the photon energy allows us to determine the inner potential V_0 to be ~ 17 eV (see also Fig. 2), which is used to convert the photon energy to k_z in Fig. 1f. Note that here the k_z band dispersion is directly related to bulk-type altermagnetic band splitting, according to Fig. 1d. In the ab initio calculations, we find that the altermagnetic splitting in CrSb is maximized along the in-plane $\bar{\Gamma} - \bar{M}$ direction at $k_z \sim 0.25c^*$, with a magnitude of ~ 1.0 eV. The k_z position where the altermagnetic splitting is maximized is close to the midpoint between two nodal planes at $k_z = 0$ and $0.5c^*$, which is likely related to the detailed crystal structure of CrSb, although such a coincidence is not enforced by any specific symmetry.

The k_z dependence of bulk-type altermagnetic splitting.

The k_z -dependent band splitting indicates the bulk-type altermagnetism in CrSb. In Figs. 2a-c, we show the valence bands taken with three representative photon energies (80, 68, and 90 eV) along the $\bar{\Gamma} - \bar{M}$ direction (more data are included in Fig. S8 in [62]). For the 80 eV photons (corresponding to $k_z \sim 0.28c^*$) in Fig. 2a, two sets of hole bands centered at $\bar{\Gamma}$ can be observed with an energy splitting up to 1.0 eV near E_F . By contrast, only one hole band can be observed near E_F under 68 eV (Fig. 2b, $k_z \sim 0$) and 90 eV (Fig. 2c, $k_z \sim 0.5c^*$) photons. These changes

in band dispersion with photon energies can be attributed to different k_z 's, as discussed above. In addition, the photoexcitation probability for the probed valence bands can also vary with the photon energy and the electron energy/momentum, leading to different photoemission intensity. The valence bands can be better visualized by taking the second derivatives, as shown in Figs. 2d-f. Such a k_z -dependent band splitting is consistent with the expected altermagnetic splitting illustrated in Fig. 1d. To make quantitative comparison, we performed ab initio calculations from DFT incorporating both the altermagnetism and SOC (AM with SOC), as shown in Figs. 2g-i. The calculations can well reproduce the experimental band structure, including the hole-type valence bands near E_F and a bundle of bands from -1 eV to -3 eV. Most importantly, the observed k_z -dependent splitting near E_F shows good agreement with the ab initio results, as indicated by the green arrows in Figs. 2d,g. The calculations in Figs. 2g-i further show that the split bands at $k_z = 0.28c^*$ exhibit strong spin polarization (red and blue curves), while the $\langle S_z \rangle$ polarization at the $k_z = 0$ and $k_z = 0.5c^*$ planes is strictly zero (black color), protected by the $[C_2^s||M_z]$ symmetry.

The altermagnetic order is essential for the observed band splitting, while the SOC plays a relatively minor role. To see this, we present DFT calculations at $k_z = 0.28c^*$ without considering altermagnetism [nonmagnetic (NM) with SOC, Fig. 2j] or SOC (AM without SOC, Fig. 2k). Comparing Figs. 2j,k with Fig. 2g, it is clear that the altermagnetism is critical to yield the observed band structure, while the influence from SOC is much weaker. The clear difference between Fig. 2g and Fig. 2j, when comparing with experimental spectra in Fig. 2d, provides direct evidence for the altermagnetic order from the band dispersion.

In general, spin is a good quantum number in altermagnets. When SOC comes into play, the SU(2) symmetry is broken and the bands with opposite spins will couple to each other, making S_z not a good quantum number. Indeed, if the SOC in CrSb were strong, it would transform the aforementioned nodal planes into an experimentally observable nodal line along the $\Gamma - A$ direction [40]. However, the bands crossing E_F in CrSb are mainly contributed by the 3d orbitals on Cr, which have weak SOC. It is therefore natural to expect that SOC has only small impact over the band structure near E_F (comparing Figs. 2g,k). By calculating the expectation value of \hat{S}_z , as shown in Fig. 2g, we find that the spin quantum number near E_F can indeed be approximated as a half-integer ($\pm\frac{1}{2}$). However, far below E_F where appreciable contributions from Sb 5p orbitals are present, e.g., $E \sim -2$ eV, the inclusion of SOC makes $\langle S_z \rangle$ deviate from $\pm 1/2$ appreciably and leads to noticeable in-plane spin polarization (see Fig. S12 in [62]). Another effect from SOC is the tiny band splitting at $k_z = 0$ and concomitant non-zero in-plane spin components $\langle S_x \rangle$ and $\langle S_y \rangle$ (see Fig. S7 and Fig. S12 in [62]), which is called weak altermagnetism in [13]. Such small splitting cannot be resolved in our experiments (comparing Figs. 2e,h).

The k_x - k_z map at $E = -0.5$ eV with fine k_z steps is shown in Fig. 2l; its second derivative and the calculated contour from DFT are displayed in Figs. 2m and 2n, respectively. Along the $P - Q$ momentum direction as defined in [51] (also labelled in Figs. 2l-n), the raw data already show a double-string feature (see arrow in Fig. 2l) with closed ends at both P and Q points, which can be better identified from the second derivative in Fig. 2m. The experimental results and DFT calculations agree quite well: the altermagnetic splitting, i.e., the separation between the two strings, is close to zero at $k_z = 0$ and gradually increases to its maximal value at $k_z \sim 0.25c^*$ (marked by arrows in Figs. 2l-n), eventually decreasing to zero at $k_z = 0.5c^*$. Our observed splitting along the $P - Q$ direction is overall consistent with the previous ARPES study from (100)-oriented CrSb films [51], although the measurement geometries are different. Our k_z -dependent study unambiguously confirms the bulk-type altermagnetic splitting in CrSb.

The in-plane symmetry of g -wave altermagnetism.

The in-plane momentum dependence of the band splitting provides direct evidence for the g -wave altermagnetism in CrSb. Fig. 3a shows the k_x - k_y map at $E = -0.65$ eV taken with 80 eV photons ($k_z \sim 0.28c^*$), where the flower-like hole-type pockets centered at $\bar{\Gamma}$ can be observed. The

constant-energy contours from ab initio calculations are overlaid on top in Fig. 3a, which agree well with the experimental data. Based on the spin group symmetry analysis, the spin-resolved contours have three-fold rotational symmetry, and the bands with different spins are related by a 60° rotation, leading to the observed six-fold flower-like pockets in the spin-integrated ARPES. Since the photoemission intensity near E_F is very low under 80 eV photons, we further show the Fermi surface map taken with 105 eV photons in Fig. 3b, which corresponds to $k_z \sim 0.2c^*$. Here the six-fold flower-like pockets expected from DFT calculations are clearly visible from the raw data, highlighting the large altermagnetic splitting right at E_F . Fig. 3c shows energy-momentum cuts taken with 80 eV photons at a series of representative θ angles, where θ is the azimuthal angle between the momentum \mathbf{k} and the $\bar{\Gamma} - \bar{K}$ direction, defined in Fig. 3a. The results clearly demonstrate the presence (absence) of altermagnetic band splitting along $\bar{\Gamma} - \bar{M}$ ($\bar{\Gamma} - \bar{K}$), as well as the gradual evolution of the splitting between these two directions. These experimental results are consistent with the corresponding spin-resolved band structures from ab initio calculations in Fig. 3d (see Fig. S9 in [62] for more details).

To quantitatively analyze the in-plane dependence of altermagnetic splitting, we also extract the momentum distribution curves (MDCs) at $E = -0.6$ eV from Fig. 3c and plot them in Fig. 3e. The MDCs are then fitted with two Gaussian peaks (see Fig. S10 in [62] for details) to yield the momentum splitting (Δk) as a function of θ (Fig. 3f). The momentum splitting agrees well with the ab initio calculation (see also Fig. S10 in [62]), including the $|\sin(3\theta)|$ -like functional form and the magnitude of splitting, although small deviations are likely present due to the experimental uncertainty or inaccuracy in calculations. We mention that the bulk-type g -wave altermagnetism only requires a six-fold in-plane symmetry in the magnitude of the band splitting, although the exact location of the nodal planes (along either $\bar{\Gamma} - \bar{K}$ or $\bar{\Gamma} - \bar{M}$) is still dependent on the details of the lattice [9].

Evidence of spin polarization from spin-resolved ARPES.

To verify the spin polarization of the altermagnetically split bands, separate spin-resolved ARPES measurements were performed along the $\bar{\Gamma} - \bar{M}$ direction with 80 eV photons ($k_z = 0.28c^*$), where the splitting is nearly maximized. Before spin-resolved measurements, the spin-integrated spectrum is checked first (Fig. 4a) and its second derivative (Fig. 4b) shows two sets of hole pockets near $\bar{\Gamma}$ from altermagnetism, similar to those in Figs. 2a,d. The different data quality in Fig. 4a and Fig. 2a can be attributed to different experimental conditions.

Figure 4c shows the spin-resolved MDCs taken along the white dashed cut in Figs. 4a,b. Here the spin detector measures the out-of-plane spin component (S_z), and the spin-up (spin-down) MDC is shown as red (blue) curve, respectively. It is clear that both spin-up and spin-down MDCs exhibit a double-peak structure with large broadening, corresponding to the spin-up and spin-down bands labelled in Fig. 4b. The obvious shifting of the peak center from spin-up to spin-down MDCs directly reflects the spin splittings expected from the altermagnetism in CrSb. Based on the calibrated Sherman function from Au(111), the corresponding spin polarization is extracted and shown in Fig. 4d. Ideally, for a single altermagnetic domain with small momentum broadening, the spin polarization along this momentum cut would be nearly 100% and exhibit a up-down-up-down pattern (or down-up-down-up, depending on the domain orientation), according to DFT calculations shown in Fig. 2g. However, the spin polarization extracted experimentally is much smaller (Fig. 4d), particularly for the inner hole pocket. There are two possible reasons for the reduced spin polarization: first, the probed area likely contains two domains with opposite spin splittings, leading to significant reduction of spin polarization, which was also observed in MnTe [13]. Note that the mixing of different domains in CrSb does not affect the spin-integrated ARPES spectra, due to the Néel vector aligning along the c axis, but the in-plane oriented Néel vector in MnTe can lead to different spin-integrated ARPES spectra for different domains [13]. Second, the large momentum broadening in the ARPES data can further reduce the spin polarization due to

overlap of opposite-spin bands. Nevertheless, our direct observation of appreciable spin polarizations in the altermagnetically split bands and their consistencies with the DFT calculations provide strong support for the altermagnetic spin splittings in CrSb.

Mechanism behind the large altermagnetic splitting.

Although the altermagnetic band splitting can be characterized by its corresponding spin group symmetry, its amplitude is dependent on the chemical bonding strength in real material. In this section, we construct a microscopic TB model to delve into the mechanism behind the large altermagnetic splitting in CrSb. Based on orbital analysis of the electronic band structure of CrSb, we find that the set of bands intersecting E_F is primarily contributed by the d_{xz} , d_{yz} , d_{xy} , and $d_{x^2-y^2}$ orbitals on Cr, which are hybridized with the p orbitals on Sb (Details can be found in Section 1 of [62]). It is important to note that both (d_{xz}, d_{yz}) and $(d_{xy}, d_{x^2-y^2})$ share the same symmetry property (the irreducible representation E_g) under the site symmetry of Cr (point group D_{3d}). Therefore, one E_g per Cr atom is sufficient to construct the effective model. A comprehensive derivation of the TB model is provided in Section 1 of [62]. Ignoring SOC, the model can be formally expressed as follows,

$$H(\mathbf{k}) = \begin{bmatrix} H^\uparrow(\mathbf{k}) & 0_{4 \times 4} \\ 0_{4 \times 4} & H^\downarrow(\mathbf{k}) \end{bmatrix} = \sum_{i=0,3} \sum_{j,m=0,1,2,3} f_{ijm}(\mathbf{k}) \Gamma_{ijm} \quad (1)$$

where $\Gamma_{ijm} = s_i \otimes \sigma_j \otimes \tau_m \equiv s_i \sigma_j \tau_m$. The Pauli matrices $s_{i=0,1,2,3}$ (or σ_i or τ_i) are used here to represent the space of spin (or the two sublattices Cr₁ and Cr₂ or the two orbitals ϕ_1 and ϕ_2 about E_g).

By incorporating all the spin group symmetries and considering the kinetic hopping terms up to the 3NN sites, we have found that both the NN and the NNN hopping terms preserve the translational spin-flip operation $[C_2^s || \vec{t}]$ [62]. It indicates that neither the NN nor the NNN hopping results in an altermagnetic spin splitting (see Fig. 1a for illustration of NN, NNN and 3NN hoppings). It is only when we take into consideration the 3NN terms that the altermagnetic splitting occurs. As demonstrated in [62], there are five 3NN terms in Eq. 1, i.e. Γ_{011} , Γ_{013} , Γ_{010} , Γ_{311} and Γ_{313} , and their coefficients are

$$\begin{aligned} f_{011}(\mathbf{k}) &= 2\sqrt{3}(q_4 - q_1) \sin^2\left(\frac{k_1}{2}\right) \cos\left(\frac{k_3}{2}\right), \\ f_{013}(\mathbf{k}) &= 2(q_4 - q_1) \sin^2\left(\frac{k_1}{2}\right) \cos\left(\frac{k_3}{2}\right), \\ f'_{010}(\mathbf{k}) &= 2(q_1 + q_4) \cos\left(\frac{k_3}{2}\right) [2 \cos(k_1) + 1], \\ f_{311}(\mathbf{k}) &= 3(q_2 + q_3) \sin(k_1) \sin\left(\frac{k_3}{2}\right), \\ f_{313}(\mathbf{k}) &= \sqrt{3}(q_2 + q_3) \sin(k_1) \sin\left(\frac{k_3}{2}\right), \end{aligned} \quad (2)$$

where q_i 's ($i = 1, 2, 3, 4$) are the independent 3NN hopping parameters between Cr atoms at $R_1 = (0, 0, 0)$ and $R_2 = (1, 1, \frac{1}{2})$, as defined below [62]

$$\begin{aligned} q_1 &= \langle \phi_1, Cr_1, R_1 | \hat{H} | \phi_1, Cr_2, R_2 \rangle, \\ q_2 &= \langle \phi_1, Cr_1, R_1 | \hat{H} | \phi_2, Cr_2, R_2 \rangle, \\ q_3 &= \langle \phi_2, Cr_1, R_1 | \hat{H} | \phi_1, Cr_2, R_2 \rangle, \\ q_4 &= \langle \phi_2, Cr_1, R_1 | \hat{H} | \phi_2, Cr_2, R_2 \rangle. \end{aligned} \quad (3)$$

The first three 3NN terms in Eq. 2, i.e., $f_{011}(\mathbf{k})\Gamma_{011}$, $f_{013}(\mathbf{k})\Gamma_{013}$ and $f'_{010}(\mathbf{k})\Gamma_{010}$, preserve the $[C_2^s || \vec{t}]$ symmetry, and they do not give rise to any altermagnetic splitting. In contrast, the last two

3NN terms $f_{311}(\mathbf{k})\Gamma_{311}$ and $f_{313}(\mathbf{k})\Gamma_{313}$, which are proportional to $q_2 + q_3$, break both $[T\|P]$ and $[C_2^s\|\vec{t}]$ symmetries, leading to the altermagnetic band/spin splitting.

Table 1: Values of the 3NN hopping parameters. The parameters in the second row are the ones used in the fitted eight-band TB model. The parameters in the third and fourth rows indicate contributions of the direct hopping (DH) and assistant hopping (AH) processes obtained from DFT calculations. The last row is the total hopping (TH) after summation of the direct and assistant hoppings. The energy unit is eV.

Parameter	q_1	$q_2 + q_3$	q_4
TB	-0.0184	0.1950	0.1942
DFT(DH)	0.0050	0.0214	-0.0660
DFT(AH)	-0.0234	0.1516	0.2602
DFT(TH)	-0.0184	0.1730	0.1942

By fitting the band structure from DFT calculations, especially along the $\bar{\Gamma} - \bar{M}$ direction near E_F , we obtain all the free parameters used in the TB model (the resulting band dispersion of the TB model is shown in Fig. 5b). We find that the fitted 3NN hopping parameters, especially $q_2 + q_3$ that gives rise to the spin splitting, are of the similar magnitude as the NNN hoppings (see Table 2 in [62]), which is counterintuitive. Indeed, d orbitals are usually very local, and the direct 3NN hopping should be very small. This is further confirmed by the DFT calculations, as shown in Table 1. In the section 2 of [62], our additional analysis based on the Wannier calculations show that the strong 3NN hoppings are dominated by a second-order hopping process mediated by Sb. In other words, the p orbitals on Sb assist the 3NN hopping between d orbitals on Cr. As tabulated in Table 1, the amplitude of $q_2 + q_3$ that arises from the direct (DH) and assistant hopping (AH) processes are about 21 and 152 meV, respectively. Their total contribution (TH) is indeed very close to the one used in the TB model. Therefore, the Sb ions between the two Cr sublattices play a crucial role for the surprisingly large 3NN hopping and hence the strong altermagnetic splitting in CrSb. These results imply that the altermagnetic splitting in CrSb can be tuned by pressure or strain, which can strongly modify the hopping processes assisted by Sb ions.

The band dispersions with $q_1 + q_4$ or $q_2 + q_3$ values reduced to half of the values in Fig. 5b are displayed in Fig. 5c and Fig. 5d, respectively. These results show that while $q_1 + q_4$ controls the overall bandwidth, $q_2 + q_3$ dictates the altermagnetic splitting within one set of band. Due to the multiorbital nature of CrSb, it is useful to define two types of spin splittings: the altermagnetic splitting within one set of band as ΔE_1 and the splitting of opposite-spin bands closest to E_F as ΔE_2 - their values at the U point, i.e., the midpoint between $\bar{\Gamma}$ and \bar{M} in the $k_z = 0.28 c^*$ plane, are labelled in Figs. 5b-d. While ΔE_1 has a simple physical meaning, ΔE_2 is directly relevant to the spin polarization near E_F (and hence the spintronic applications). In Figs. 5e,f, we systematically investigate the evolution of ΔE_{1U} and ΔE_{2U} as a function of $q_2 + q_3$ and $q_1 + q_4$. Our results show that ΔE_{1U} is approximately proportional to the magnitude of $q_2 + q_3$ and is almost independent of $q_1 + q_4$ in this parameter region, as expected by our TB model. On the other hand, ΔE_{2U} becomes dependent on $q_1 + q_4$ when $q_2 + q_3$ becomes larger than ~ 0.1 eV. This is because when $q_2 + q_3$ becomes large, the top conduction bands with similar spin splitting will now cross E_F (see Fig. 5c), reducing ΔE_{2U} accordingly. This implies that for a multiorbital system like CrSb, a careful tuning of different band parameters is necessary to generate maximal spin splitting near E_F . Figs. 5g,h show the evolution of ΔE_1 and ΔE_2 along $\bar{\Gamma} - \bar{M}$ at $k_z = 0.28 c^*$, by increasing the numerical values of $\{q_i\}$ while keeping a fixed ratio among them (corresponding to the grey dashed lines in Figs. 5e,f). These calculations, which can simulate the process of uniform compression, indicate a clear and monotonic increase in the magnitude of altermagnetic splitting under hydrostatic pressure.

Discussion

It is interesting to compare CrSb with MnTe, another bulk-type g -wave altermagnet with similar crystal structure [13]. There are several important differences between these two systems. Firstly, the $3d$ spins in CrSb are aligned along the c axis, in contrast to the in-plane $3d$ spins in MnTe. This eliminates multiple band splittings caused by the different in-plane domains as reported in MnTe [13, 15, 63] and allows for clear identification of altermagnetic splitting in CrSb. Secondly, the valences of Cr and Mn should be different, leading to different fillings of the $3d$ valence bands and hence distinct ground states (metallic in CrSb and semiconducting in MnTe). Finally, the lattice constant c in CrSb (5.44 Å) is considerably smaller than that of MnTe (6.75 Å), which, together with the stronger electron correlation in MnTe with $U \sim 4.8$ eV [13], gives rise to stronger electron hopping and hence larger altermagnetic splitting up to 1.0 eV near E_F in CrSb. By contrast, the observed altermagnetic splitting in MnTe is $\lesssim 0.5$ eV and is located far below E_F , which is mainly derived from Te p orbitals [12, 13]. We note that our TB model might not be directly applicable to MnTe, due to different orbital character and nature of magnetism.

The mechanism of large altermagnetic splitting in CrSb can be further illustrated by comparison with VNb_3S_6 , which is another proposed bulk-type g -wave altermagnet with the identical spin group symmetry as CrSb and MnTe [10]. Since the magnetic moments of V are antiparallel between two neighboring layers, the altermagnetic splitting in VNb_3S_6 also originates from the interlayer hopping. Yet its much larger lattice constant $c = 12.17$ Å [64] and weak interlayer coupling between V and NbS_2 layers result in a very small splitting of a few tens of meV (see Fig. S11 in [62]).

The large bulk-type g -wave altermagnetic splitting at E_F in CrSb provides interesting opportunities to explore novel superconducting proximity effects at the interfaces between metallic altermagnets and conventional superconductors. For instance, it has been theoretically proposed that the interface between a conventional superconductor and a planar d -wave altermagnet can induce finite-momentum pairing [44], and their planar Josephson junctions can exhibit orientation-dependent $0-\pi$ oscillations [45]. In contrast, due to the three-dimensional spin-degenerate nodal planes of CrSb, both planar and vertical Josephson junctions composed of CrSb could exhibit similar (or even richer) superconducting properties. For example, the vertical Josephson junction could achieve damped oscillating pairing along any direction non-parallel to the nodal planes, facilitating the toggling of finite-momentum pairing on and off by controlling the orientation of the interface. Therefore, our work will motivate future theoretical and experimental studies to explore such intriguing phenomena.

In summary, we present direct spectroscopic evidence of bulk-type g -wave altermagnetism in CrSb from high-resolution synchrotron-based ARPES and spin-resolved ARPES measurements. Our systematic k_z and in-plane momentum dependent study confirms a large altermagnetic splitting up to 1.0 eV near E_F , which is in good agreements with the DFT calculations. The spin polarization of split bands is further verified by spin-resolved ARPES measurements. Our TB model analysis reveals that the altermagnetic splitting arises mainly from the 3NN hopping of Cr $3d$ electrons mediated by Sb $5p$ orbitals, highlighting the important role of electronic coupling between magnetic and nonmagnetic ions. The insight can be important for finding/tuning altermagnetic materials with enhanced properties. The large altermagnetic splitting near E_F , together with the high ordering temperature up to 700 K in CrSb, paves the way for exploring emergent phenomena and practical applications based on altermagnets.

Note: during the review process of this paper, we became aware of other independent ARPES works on CrSb posted on arXiv [65–67], which also support the altermagnetism in CrSb.

Methods

Single crystal growth and characterizations.

Single crystals of CrSb were grown using an antimony flux. The elements were combined in a molar ratio of Cr:Sb of 2:3, and sealed in an evacuated quartz tube. The tube was heated up to 1150 °C and held at this temperature for 20 hours, before being cooled down slowly to 700 °C and centrifuged to remove the excess antimony flux. The lateral size of the single crystals is typically 1x1 mm². The chemical composition of the crystals was confirmed by energy dispersive X-ray spectroscopy. The crystal structure was checked by XRD measurements (Fig. 1b and Fig. S5b in [62]). The temperature-dependent resistivity was measured using a Physical Property Measurement System (PPMS), and it shows metallic behavior with no phase transition from 300 K down to 1.8 K (Fig. S5a in [62]), consistent with previous reports [68]. The cleaved single crystals were also characterized by core-level photoemission measurements, which show expected core level peaks from Cr 3*p* and Sb 4*d* electrons (Fig. S5c in [62]), without any trace of impurities.

Synchrotron-based ARPES measurements.

The spin-integrated ARPES measurements were carried out at the BLOCH beamline in Max IV Lab (Sweden) and the BL03U beamline at Shanghai Synchrotron Radiation Facility (SSRF, China). The typical energy resolution was set to ~20 meV and the measurement temperature is ~20 K. The typical beam spot is ~15×15 μm² for the BLOCH beamline and ~50×50 μm² for the BL03U beamline. The ARPES measurements were performed on the (001)-oriented surface, which was cleaved *in-situ* at measurement temperature and under ultrahigh vacuum ($< 5 \times 10^{-11}$ mbar). All ARPES data in our manuscript were taken with horizontally polarized photons.

The spin-resolved ARPES measurements were conducted at the APE-LE beamline in Elettra Sincrotrone Trieste (Italy). The typical energy and angular resolutions are ~100 meV and ~1.5°, respectively. The measurement temperature is ~15 K. The typical beam spot is ~150×50 μm². The Sherman function of the spin detector is 0.3, calibrated by the Rashba-split surface states from Au(111) right before the experiment. The spin-resolved ARPES measurements were achieved through VESPA (Very Efficient Spin Polarization Analysis), which consists of two very low energy electron diffraction (VLEED)-based scattering chambers and is able to measure all three spin components of the photo-emitted electrons [69].

Ab initio calculations.

The DFT calculations were performed using the Vienna Ab initio Simulation Package (VASP) [70, 71]. The Perdew, Burke and Ernzerhoff (PBE) parametrization of generalized gradient approximation (GGA) to the exchange-correlation functional was employed [72]. We performed calculations with different choices of the coulomb repulsion U (see Fig. S6 in [62]), and we found that $U = 0$ shows the best agreement with the experimental results. Therefore, U is set to zero in all calculations, unless noted otherwise. An energy cutoff of 345 eV and 11×1×9 Γ -centered K-mesh were employed to converge the total energy to 1 meV/atom. The band structure obtained from PBE method were fitted to a tight-binding model Hamiltonian with maximally projected Wannier function method, which was then used to calculate the Fermi surface with `wannier_tools` package. To understand the underlying origin of altermagnetic splitting, calculations with either SOC or AM turned off, i.e., AM without SOC or NM with SOC, were both performed (see Fig. S7 in [62]). The results show that altermagnetism plays a dominant role in the observed band structure, while the SOC effect is not very important.

Data Availability

All the source data accompanying this manuscript have been deposited in the Figshare repository, accessible via <https://doi.org/10.6084/m9.figshare.25865749>.

Acknowledgments This work is supported by the National Key R&D Program of China (Grant No. 2023YFA1406303, No. 2022YFA1402200), the Key R&D Program of Zhejiang Province, China (2021C01002), the National Natural Science Foundation of China (No. 12174331, No. 12204159, No.

12374163, No. 12350710785) and the State Key project of Zhejiang Province (No. LZ22A040007). We acknowledge MAX IV Laboratory for time on Beamline BLOCH under Proposal 20230343. Research conducted at MAX IV, a Swedish national user facility, is supported by the Swedish Research council under contract 2018-07152, the Swedish Governmental Agency for Innovation Systems under contract 2018-04969, and Formas under contract 2019-02496. We also acknowledge Elettra Sincrotrone Trieste for time on Beamline APE-LE under Proposal 20240269. This work has been partly performed in the framework of the nanoscience foundry and fine analysis (NFFA-MUR Italy Progetti Internazionali) facility. Part of this research used beamline 03U of the Shanghai Synchrotron Radiation Facility, which is supported by the ME2 project under Contract No. 11227902 from the National Natural Science Foundation of China. We would like to thank Prof. Dawei Shen, Dr. Zhengtai Liu, Dr. Balasubramanian Thiagarajan, Dr. Mats Leandersson, Dr. Indrani Kar, Ms. Jiayi Lu and Prof. Guanghan Cao for experimental help. We are also grateful to Prof. Yulin Chen, Prof. Chang Liu, Mr. Qi Jiang and Prof. Xin Lu for useful discussions. Some of the images in the paper were created using VESTA software [73].

Author contributions The project was designed by Y. L. Single crystal growth and characterization was done by S. Y., J. L., J. Z., H. Y. and Y. Z, with help from S. C. and Y. S.. The ARPES measurement was performed by G. Y., with help from H. Z., W. Z., Z. P., Yifu Xu, A. J., J. F., I. V., W. Z., M. Y., L. Y., M. S. and Y. L. ARPES data analysis was done by G. Y. and Y. L., with help from Z. L. and Yuanfeng Xu. Ab initio calculations and tight-binding model analysis were carried out by Z. L. and Yuanfeng Xu. L.-H. H. and M. S. contribute to the discussion. The manuscript was prepared by G. Y., Z. L., Yuanfeng Xu and Y. L., with inputs from all other coauthors. All authors discussed the results and commented on the manuscript.

Competing interests The authors declare no competing interests.

Additional information Supplementary Information is available for this paper.

References

- [1] Wu, C., Sun, K., Fradkin, E. & Zhang, S.-C. Fermi liquid instabilities in the spin channel. *Phys. Rev. B* **75**, 115103 (2007).
- [2] Hayami, S., Yanagi, Y. & Kusunose, H. Momentum-dependent spin splitting by collinear antiferromagnetic ordering. *Journal of the Physical Society of Japan* **88**, 123702 (2019).
- [3] Smejkal, L., Gonzalez-Hernandez, R., Jungwirth, T. & Sinova, J. Crystal time-reversal symmetry breaking and spontaneous Hall effect in collinear antiferromagnets. *Sci. Adv.* **6**, eaaz8809 (2020).
- [4] Hayami, S., Yanagi, Y. & Kusunose, H. Spontaneous antisymmetric spin splitting in non-collinear antiferromagnets without spin-orbit coupling. *Phys. Rev. B* **101**, 220403 (2020).
- [5] Yuan, L.-D., Wang, Z., Luo, J.-W., Rashba, E. I. & Zunger, A. Giant momentum-dependent spin splitting in centrosymmetric low-Z antiferromagnets. *Phys. Rev. B* **102**, 014422 (2020).
- [6] Mazin, I. I., Koepf, K., Johannes, M. D., González-Hernández, R. & Šmejkal, L. Prediction of unconventional magnetism in doped FeSb₂. *Proceedings of the National Academy of Sciences* **118**, e2108924118 (2021).
- [7] Ma, H.-Y. *et al.* Multifunctional antiferromagnetic materials with giant piezomagnetism and noncollinear spin current. *Nat. Commun.* **12**, 2846 (2021).

- [8] Liu, P., Li, J., Han, J., Wan, X. & Liu, Q. Spin-group symmetry in magnetic materials with negligible spin-orbit coupling. *Phys. Rev. X* **12**, 021016 (2022).
- [9] Šmejkal, L., Sinova, J. & Jungwirth, T. Beyond conventional ferromagnetism and antiferromagnetism: A phase with nonrelativistic spin and crystal rotation symmetry. *Phys. Rev. X* **12**, 031042 (2022).
- [10] Šmejkal, L., Sinova, J. & Jungwirth, T. Emerging research landscape of altermagnetism. *Phys. Rev. X* **12**, 040501 (2022).
- [11] Šmejkal, L., MacDonald, A. H., Sinova, J., Nakatsuji, S. & Jungwirth, T. Anomalous Hall antiferromagnets. *Nature Reviews Materials* **7**, 482 (2022).
- [12] Lee, S. *et al.* Broken Kramers degeneracy in altermagnetic MnTe. *Phys. Rev. Lett.* **132**, 036702 (2024).
- [13] Krempaský, J. *et al.* Altermagnetic lifting of Kramers spin degeneracy. *Nature* **626**, 517–522 (2024).
- [14] Osumi, T. *et al.* Observation of a giant band splitting in altermagnetic MnTe. *Phys. Rev. B* **109**, 115102 (2024).
- [15] Hajlaoui, M. *et al.* Temperature dependence of relativistic valence band splitting induced by an altermagnetic phase transition. Preprint at <https://arxiv.org/abs/2401.09187> (2024).
- [16] Hariki, A. *et al.* X-ray magnetic circular dichroism in altermagnetic α -MnTe. *Phys. Rev. Lett.* **132**, 176701 (2024).
- [17] Gonzalez Betancourt, R. D. *et al.* Spontaneous anomalous Hall effect arising from an unconventional compensated magnetic phase in a semiconductor. *Phys. Rev. Lett.* **130**, 036702 (2023).
- [18] Feng, Z. *et al.* An anomalous Hall effect in altermagnetic ruthenium dioxide. *Nature Electronics* **5**, 735–743 (2022).
- [19] Tschirner, T. *et al.* Saturation of the anomalous Hall effect at high magnetic fields in altermagnetic RuO₂. *APL Materials* **11**, 101103 (2023).
- [20] Bose, A. *et al.* Tilted spin current generated by the collinear antiferromagnet ruthenium dioxide. *Nature Electronics* **5**, 267–274 (2022).
- [21] Bai, H. *et al.* Observation of spin splitting torque in a collinear antiferromagnet RuO₂. *Phys. Rev. Lett.* **128**, 197202 (2022).
- [22] Karube, S. *et al.* Observation of spin-splitting torque in collinear antiferromagnetic RuO₂. *Phys. Rev. Lett.* **129**, 137201 (2022).
- [23] Fedchenko, O. *et al.* Observation of time-reversal symmetry breaking in the band structure of altermagnetic RuO₂. *Science Advances* **10**, eadj4883 (2024).
- [24] Hiraishi, M. *et al.* Nonmagnetic ground state in RuO₂ revealed by muon spin rotation. *Phys. Rev. Lett.* **132**, 166702 (2024).
- [25] Liu, J. *et al.* Absence of altermagnetic spin splitting character in rutile oxide RuO₂. Preprint at <https://arxiv.org/abs/2409.13504> (2024).

- [26] Wang, M. *et al.* Emergent zero-field anomalous Hall effect in a reconstructed rutile antiferromagnetic metal. *Nat. Commun.* **14**, 8240 (2023).
- [27] Leiviskä, M. *et al.* Anisotropy of the anomalous hall effect in thin films of the altermagnet candidate Mn_5Si_3 . *Phys. Rev. B* **109**, 224430 (2024).
- [28] Reichlova, H. *et al.* Observation of a spontaneous anomalous hall response in the Mn_5Si_3 d-wave altermagnet candidate. *Nat. Commun.* **15**, 4961 (2024).
- [29] Urata, T., Hattori, W. & Ikuta, H. High mobility charge transport in a multicarrier altermagnet CrSb . *Phys. Rev. Mater.* **8**, 084412 (2024).
- [30] Bai, Y. *et al.* Nonlinear field dependence of Hall effect and high-mobility multi-carrier transport in an altermagnet CrSb . Preprint at <https://arxiv.org/abs/2409.14855> (2024).
- [31] Šmejkal, L., Hellenes, A. B., González-Hernández, R., Sinova, J. & Jungwirth, T. Giant and tunneling magnetoresistance in unconventional collinear antiferromagnets with nonrelativistic spin-momentum coupling. *Phys. Rev. X* **12**, 011028 (2022).
- [32] Cui, Q., Zhu, Y., Yao, X., Cui, P. & Yang, H. Giant spin-Hall and tunneling magnetoresistance effects based on a two-dimensional nonrelativistic antiferromagnetic metal. *Phys. Rev. B* **108**, 024410 (2023).
- [33] Gonzalez-Hernandez, R. *et al.* Efficient electrical spin splitter based on nonrelativistic collinear antiferromagnetism. *Phys. Rev. Lett.* **126**, 127701 (2021).
- [34] Bai, H. *et al.* Efficient spin-to-charge conversion via altermagnetic spin splitting effect in antiferromagnet RuO_2 . *Phys. Rev. Lett.* **130**, 216701 (2023).
- [35] Shao, D.-F. *et al.* Néel spin currents in antiferromagnets. *Phys. Rev. Lett.* **130**, 216702 (2023).
- [36] Zhou, Z. *et al.* Crystal design of altermagnetism. Preprint at <https://arxiv.org/abs/2403.07396> (2024).
- [37] Zhou, X. *et al.* Crystal thermal transport in altermagnetic RuO_2 . *Phys. Rev. Lett.* **132**, 056701 (2024).
- [38] Badura, A. *et al.* Observation of the anomalous Nernst effect in altermagnetic candidate Mn_5Si_3 . Preprint at <https://arxiv.org/abs/2403.12929> (2024).
- [39] Han, L. *et al.* Observation of non-volatile anomalous Nernst effect in altermagnet with collinear Néel vector. Preprint at <https://arxiv.org/abs/2403.13427> (2024).
- [40] Fernandes, R. M., de Carvalho, V. S., Birol, T. & Pereira, R. G. Topological transition from nodal to nodeless zeeman splitting in altermagnets. *Phys. Rev. B* **109**, 024404 (2024).
- [41] Li, Y.-X., Liu, Y. & Liu, C.-C. Creation and manipulation of higher-order topological states by altermagnets. *Phys. Rev. B* **109**, L201109 (2024).
- [42] Zhu, D., Zhuang, Z.-Y., Wu, Z. & Yan, Z. Topological superconductivity in two-dimensional altermagnetic metals. *Phys. Rev. B* **108**, 184505 (2023).
- [43] Brekke, B., Brataas, A. & Sudbø, A. Two-dimensional altermagnets: Superconductivity in a minimal microscopic model. *Phys. Rev. B* **108**, 224421 (2023).
- [44] Zhang, S.-B., Hu, L.-H. & Neupert, T. Finite-momentum Cooper pairing in proximitized altermagnets. *Nat. Commun.* **15**, 1801 (2024).

- [45] Ouassou, J. A., Brataas, A. & Linder, J. dc Josephson effect in altermagnets. *Phys. Rev. Lett.* **131**, 076003 (2023).
- [46] Xu, C. *et al.* Frustrated altermagnetism and charge density wave in kagome superconductor CsCr₃Sb₅ films. Preprint at <https://arxiv.org/abs/2309.14812> (2023).
- [47] Li, Y.-X. & Liu, C.-C. Majorana corner modes and tunable patterns in an altermagnet heterostructure. *Phys. Rev. B* **108**, 205410 (2023).
- [48] Zhu, Y.-P. *et al.* Observation of plaid-like spin splitting in a noncoplanar antiferromagnet. *Nature* **626**, 523–528 (2024).
- [49] Sødequist, J. & Olsen, T. Two-dimensional altermagnets from high throughput computational screening: Symmetry requirements, chiral magnons, and spin-orbit effects. *Applied Physics Letters* **124**, 182409 (2024).
- [50] Takei, W. J., Cox, D. E. & Shirane, G. Magnetic structures in the MnSb-CrSb system. *Phys. Rev.* **129**, 2008–2018 (1963).
- [51] Reimers, S. *et al.* Direct observation of altermagnetic band splitting in CrSb thin films. *Nat. Commun.* **15**, 2116 (2024).
- [52] Snow, A. I. Neutron diffraction investigation of the atomic magnetic moment orientation in the antiferromagnetic compound CrSb. *Phys. Rev.* **85**, 365–365 (1952).
- [53] Abe, S., Kaneko, T., Ohashi, M., Yoshida, H. & Kamigaki, K. Magnetic properties of CrSb. *Journal of the Physical Society of Japan* **53**, 2703–2709 (1984).
- [54] Yuan, J., Song, Y., Xing, X. & Chen, J. Magnetic structure and uniaxial negative thermal expansion in antiferromagnetic CrSb. *Dalton Trans.* **49**, 17605 (2020).
- [55] Brinkman, W. F., Elliott, R. J. & Peierls, R. E. Theory of spin-space groups. *Proceedings of the Royal Society of London. Series A. Mathematical and Physical Sciences* **294**, 343–358 (1966).
- [56] Litvin, D. & Opechowski, W. Spin groups. *Physica* **76**, 538–554 (1974).
- [57] Xiao, Z., Zhao, J., Li, Y., Shindou, R. & Song, Z.-D. Spin space groups: Full classification and applications. Preprint at <https://arxiv.org/abs/2307.10364> (2023).
- [58] Ren, J. *et al.* Enumeration and representation of spin space groups. Preprint at <https://arxiv.org/abs/2307.10369> (2023).
- [59] Jiang, Y. *et al.* Enumeration of spin-space groups: Towards a complete description of symmetries of magnetic orders. Preprint at <https://arxiv.org/abs/2307.10371>(2023).
- [60] Hüfner, S. *Photoelectron Spectroscopy: Principles and Applications*. Advanced Texts in Physics (Springer, 2003).
- [61] Sobota, J. A., He, Y. & Shen, Z.-X. Angle-resolved photoemission studies of quantum materials. *Rev. Mod. Phys.* **93**, 025006 (2021).
- [62] See online Supplementary Information.
- [63] Mazin, I. I. Altermagnetism in mnTe: Origin, predicted manifestations, and routes to detwinning. *Phys. Rev. B* **107**, L100418 (2023).

- [64] Lu, K. *et al.* Canted antiferromagnetic order in the monoaxial chiral magnets $V_{1/3}\text{TaS}_2$ and $V_{1/3}\text{NbS}_2$. *Phys. Rev. Mater.* **4**, 054416 (2020).
- [65] Zeng, M. *et al.* Observation of spin splitting in room-temperature metallic antiferromagnet CrSb. Preprint at <https://arxiv.org/abs/2405.12679> (2024).
- [66] Ding, J. *et al.* Large band-splitting in g -wave type altermagnet CrSb. Preprint at <https://arxiv.org/abs/2405.12687> (2024).
- [67] Li, C. *et al.* Topological Weyl altermagnetism in CrSb. Preprint at <https://arxiv.org/abs/2405.14777> (2024).
- [68] Suzuoka, T. An electrical resistance study of the system $(\text{Cr}_x\text{Mn}_{1-x})\text{Sb}$. *Journal of the Physical Society of Japan* **12**, 1344–1347 (1957).
- [69] Bigi, C. *et al.* Very efficient spin polarization analysis (VESPA): new exchange scattering-based setup for spin-resolved ARPES at APE-NFFA beamline at Elettra. *Journal of Synchrotron Radiation* **24**, 750–756 (2017).
- [70] Kresse, G. & Hafner, J. Ab initio molecular dynamics for liquid metals. *Phys. Rev. B* **47**, 558–561 (1993).
- [71] Kresse, G. & Joubert, D. From ultrasoft pseudopotentials to the projector augmented-wave method. *Phys. Rev. B* **59**, 1758–1775 (1999).
- [72] Perdew, J. P., Burke, K. & Ernzerhof, M. Generalized gradient approximation made simple. *Phys. Rev. Lett.* **77**, 3865–3868 (1996).
- [73] Momma, K. & Izumi, F. *VESTA3* for three-dimensional visualization of crystal, volumetric and morphology data. *Journal of Applied Crystallography* **44**, 1272–1276 (2011).

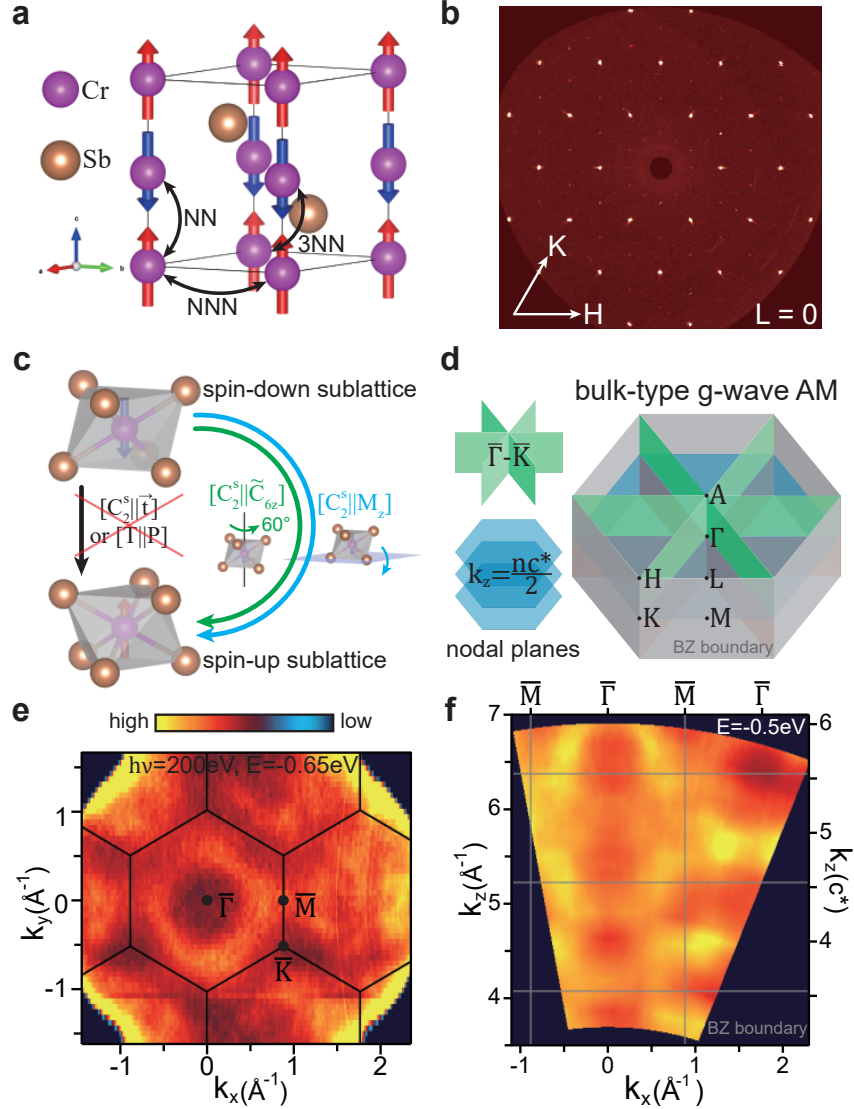


Fig. 1: Spin/lattice structure and characterization of CrSb. **a** Spin and lattice structure of CrSb. The nearest neighbor (NN), next nearest neighbor (NNN), and third nearest neighbor (3NN) Cr-Cr bonds are indicated by the black arrow lines. **b** H-K map ($L = 0$) of a (001)-oriented crystal from XRD. **c** Symmetry operations connecting the opposite-spin sublattices. **d** Left: the nodal planes corresponding to spin-group symmetries in (c). The $k_z = nc^*/2$ nodal planes, where $c^* = 2\pi/c$ and n is an integer, are protected by $[C_2^s \parallel M_z]$ combining with translation symmetry. Right: The three-dimensional Brillouin zone (BZ) with high symmetry points and nodal planes labeled. **e** The in-plane k_x - k_y map at $E = -0.65$ eV, taken with 200 eV photons (corresponding to $k_z \sim 0.5c^*$). **f** The k_x - k_z map at $E = -0.5$ eV along $\bar{\Gamma} - \bar{M}$ (k_x). The black hexagons in (e) and grey rectangles in (f) label the BZ boundaries. The surface BZ for (001)-oriented CrSb, which is the projection of three-dimensional BZ onto the (001) surface, is labelled in (e) with the high-symmetry points $\bar{\Gamma}$, \bar{M} and \bar{K} . The color bar for image plots in (e,f) is indicated.

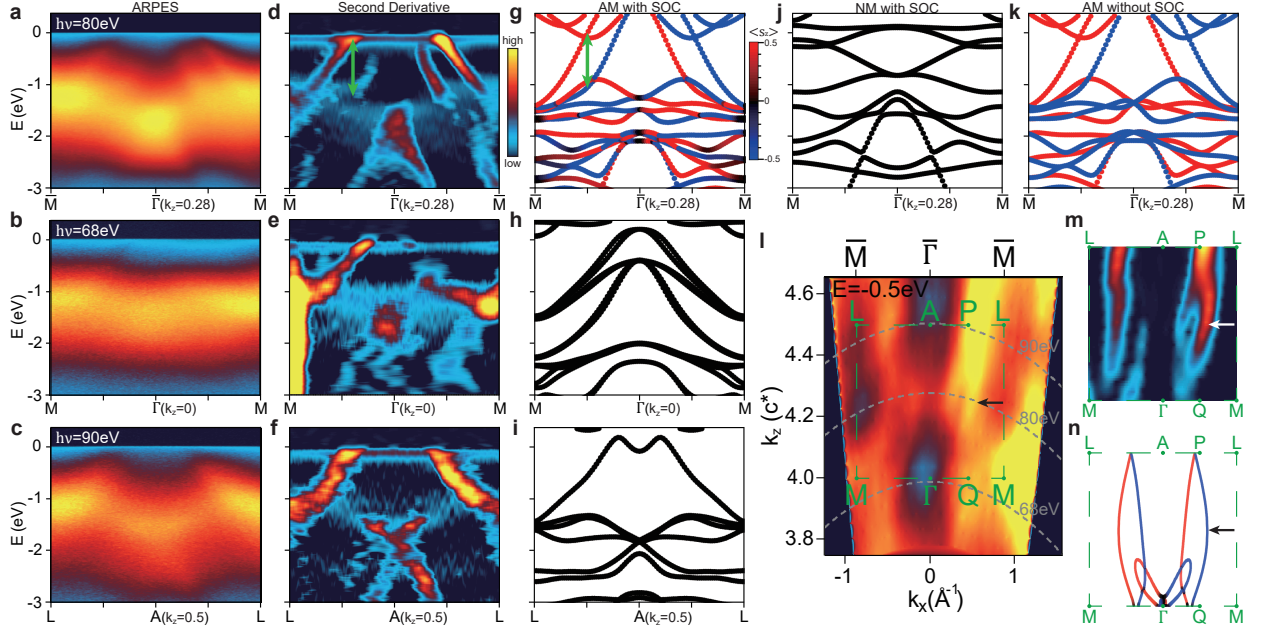


Fig. 2: The k_z dependence of altermagnetic splittings along the in-plane $\bar{\Gamma} - \bar{M}$ direction. **a,b,c** ARPES spectra taken with 80 eV (a), 68 eV (b), 90 eV (c) photons. **d,e,f** The second derivatives of the ARPES spectra corresponding to (a-c). **g,h,i** Spin-resolved band structure from DFT calculations considering both AM and SOC at $k_z = 0.28c^*$ (g), 0 (h) and $0.5c^*$ (i), for comparison with experimental data on the left. The green arrows in (d,g) highlight the altermagnetic band splittings. **j,k** DFT calculations at $k_z = 0.28c^*$, considering only SOC (j, NM with SOC) or altermagnetism (k, AM without SOC), for comparison with (g). **l** The k_x - k_z map at $E = -0.5$ eV. The green dashed rectangle marks half of the BZ from $M - \bar{\Gamma} - M$ ($k_z = 0$) to $L - A - L$ ($k_z = 0.5c^*$). Grey dashed curves indicate the k_x - k_z cuts corresponding to (a-c). **m** The second derivative of the k_x - k_z map within the green dashed rectangle of (l). **n** The k_x - k_z contour at $E = -0.5$ eV from DFT, for comparison with (l,m). Note that the small feature near $\bar{\Gamma}$ in (n) is not observed experimentally. Arrows in (l-n) mark the altermagnetic splitting maximized near $k_z = 0.25c^*$. The colors of the curves in DFT calculations indicate the spin polarization [color bar shown in (g)].

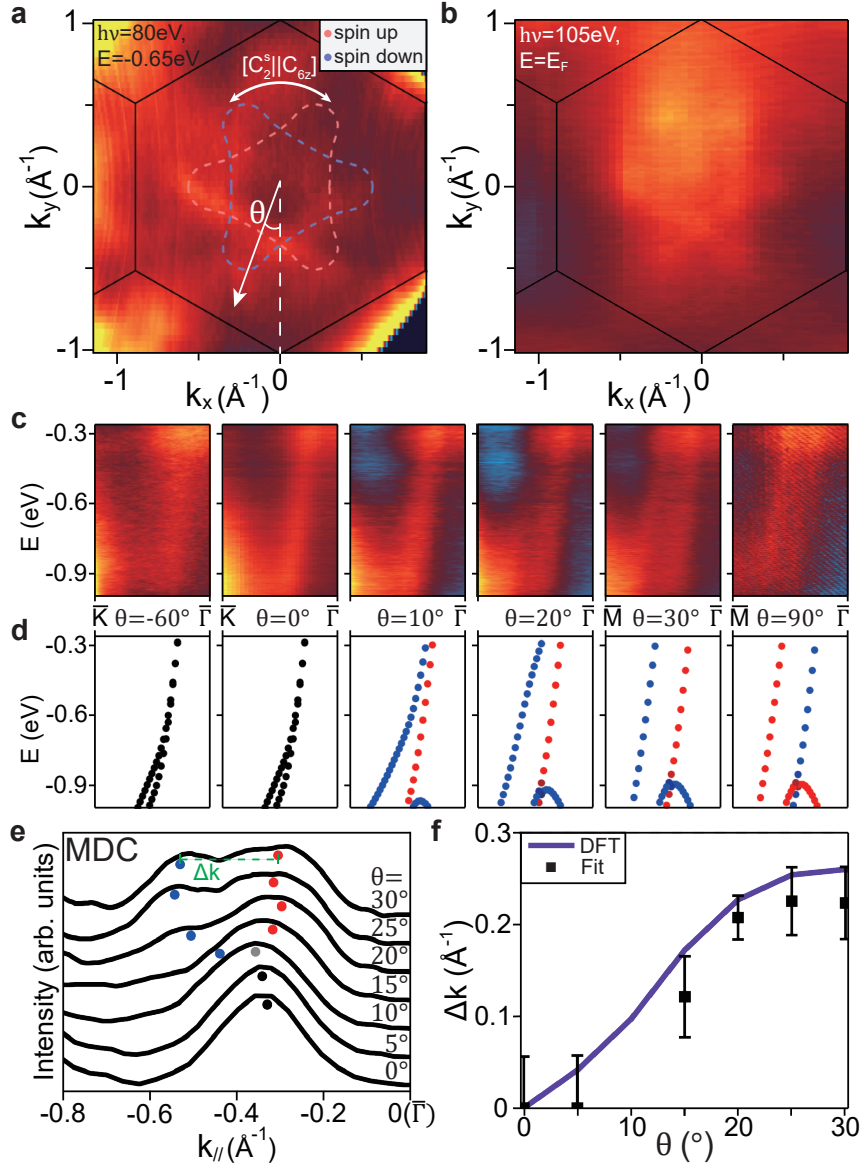


Fig. 3: The in-plane altermagnetic splitting away from the nodal planes. **a** The constant-energy k_x - k_y map at -0.65 eV, taken with 80 eV photons and using the deflection mode ($k_z \sim 0.28c^*$). The corresponding constant-energy contours from DFT calculations are overlaid on top as dashed curves. **b** The Fermi surface map taken with 105 eV photons, corresponding to $k_z \sim 0.2c^*$. **c** The energy-momentum cuts taken with 80 eV photons for a few representative θ values [defined in **(a)**]. **d** Band structure from DFT for comparison with **(c)**. The momentum range for each plot in **(c,d)** is from the BZ boundary (left) to $\bar{\Gamma}$. The curve colors in **(a,d)** indicate the spin polarization. **e** MDCs at $E = -0.6$ eV for θ from 0° to 30° . Dots indicate fitted peak positions. **f** The extracted altermagnetic momentum splitting Δk (black boxes with error bars) from **(e)**, in comparison with DFT calculation (purple curve).

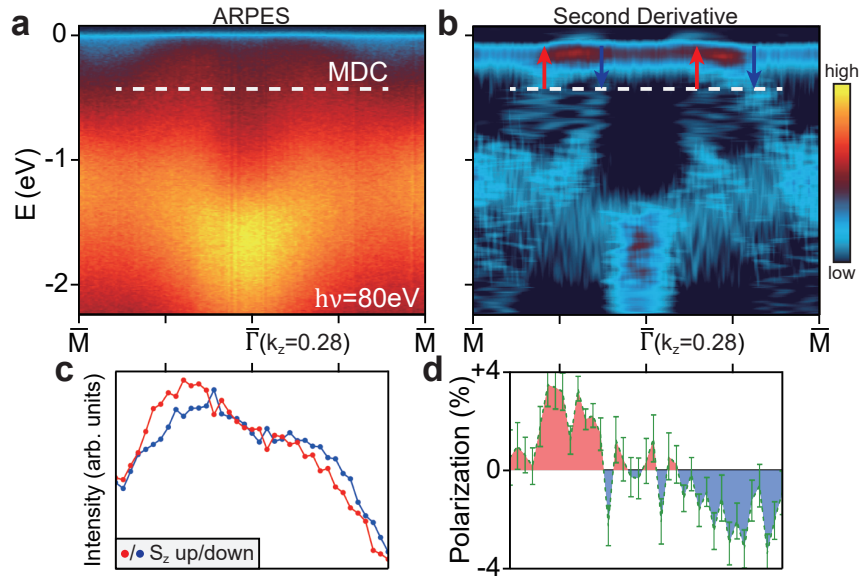


Fig. 4: Evidence of spin polarization from spin-resolved ARPES measurements. **a** Spin-integrated ARPES spectrum along $\bar{\Gamma} - \bar{M}$ taken with 80 eV photons, for the sample used for spin ARPES measurements. **b** The second derivative of **(a)**. The expected spin polarizations of the split bands near E_F are labelled by red (spin-up) and blue (spin-down) arrows. **c** Spin-resolved MDCs along the white dashed cut in **(a,b)**. The red (blue) curve indicates the spin-up (spin-down) MDC for the spin component along z , i.e., S_z . **d** The spin polarizations extracted from the spin-resolved MDCs in **(c)**. Error bars are defined as the standard error of polarization at each k point between repeated scans.

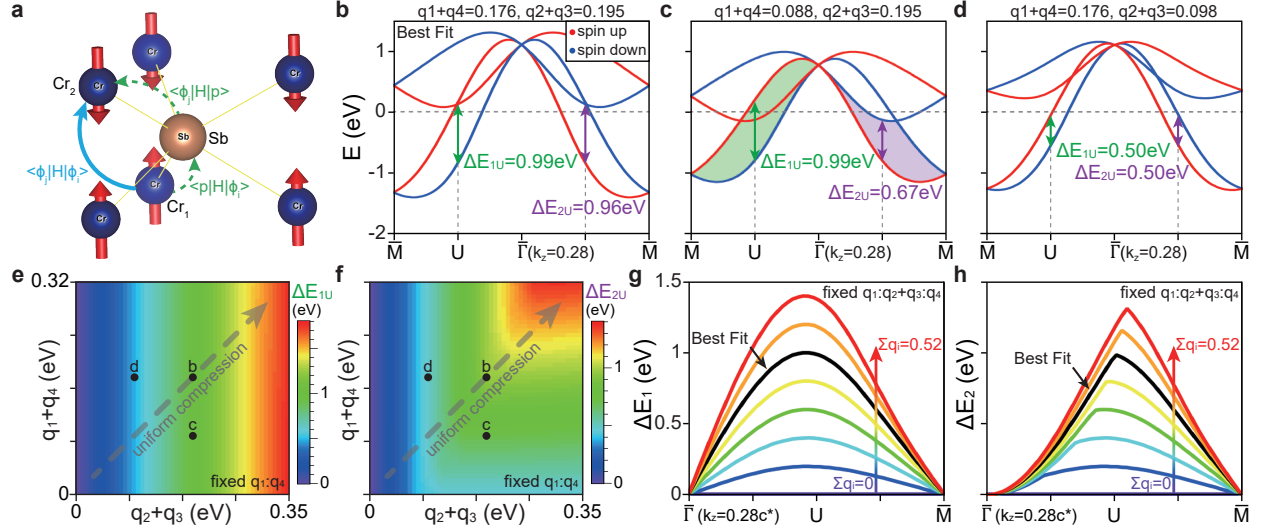


Fig. 5: Origin of the large altermagnetic splitting in CrSb. **a** The dominant hopping process between the 3NN Cr atoms at $R_1 = (0, 0, 0)$ (Cr_1) and $R_2 = (1, 1, \frac{1}{2})$ (Cr_2), which is mediated by the p orbitals on the Sb atom at $(\frac{1}{3}, \frac{2}{3}, \frac{1}{4})$. Here we use Cr_1 (Cr_2) to present the Cr sublattice with up (down) spins. **b** Band dispersions along the $\bar{\Gamma} - \bar{M}$ direction at $k_z = 0.28c^*$ obtained from the eight-band TB fit to DFT calculation. The red and blue lines represent spin-up and spin-down bands, respectively. The altermagnetic splitting within one band (ΔE_{1U}) and the splitting of opposite-spin bands closest to E_F (ΔE_{2U}) at the U point are both defined. **c, d** Band dispersions with $q_1 + q_4$ (**c**) or $q_2 + q_3$ (**d**) reducing to half of its value in (**b**). **e, f** ΔE_{1U} (**e**) and ΔE_{2U} (**f**) as a function of $q_2 + q_3$ and $q_1 + q_4$. The black dots label the positions corresponding to (**b-d**). The color bars for the image plots are shown on the right. **g, h** ΔE_1 (**g**) and ΔE_2 (**h**) along the $\bar{\Gamma} - \bar{M}$ direction at $k_z = 0.28c^*$ by increasing the value of $\sum q_i$ from 0 to 0.52 eV, where the ratio $q_1 : q_2 + q_3 : q_4$ is fixed. The black curve corresponds to the best fit to DFT (**b**).

Supplementary information for:

Three-dimensional mapping and electronic origin of large altermagnetic splitting near Fermi level in CrSb

This supplementary document contains the following parts:

- I. Details of tight-binding model analysis, which includes Section 1-3, Table 1-5 and Figs. S1-S4, S13.
- II. Additional sample characterization, which includes Fig. S5.
- III. Additional DFT calculations, which include Figs. S6, S7, S9, S11, S12.
- IV. Additional ARPES data and comparison with calculations, which include Figs. S8, S10.

1 Tight-binding Model

The magnetic crystal structure of CrSb is characterized by the magnetic space group $P6'_3/m'm'c$. As discussed in the main text, the low-energy band structure of CrSb in its magnetic phase is mainly contributed by the d orbitals on Cr, which have weak spin-orbit coupling (SOC). Therefore, we can ignore the SOC effect. In the following, we build a tight-binding Hamiltonian using its corresponding spin group symmetry to analyze the spin-splitting magnitude in the altermagnet CrSb. For each spin component in CrSb, its Hamiltonian is characterized by the spinless space group $P\bar{3}m1$ (#164), containing three generators C_{3z} , inversion P , and C_{2x} . Then, the two Hamiltonians with different spins are related by a composed symmetry $[C_2^s || \{M_z | (0, 0, \frac{1}{2})\}]$, where C_2^s is a spin-flip operation and $\{M_z | (0, 0, \frac{1}{2})\}$ is a mirror reflection.

Table 2: Occupied Wyckoff positions in the crystal structure of CrSb. For each spin sublattice, it crystallizes in the space group $P\bar{3}m1$.

Atom	Wyckoff position	Coordinates	Site symmetry
Cr ₁	1a	(0,0,0)	D_{3d}
Cr ₂	1b	$(0, 0, \frac{1}{2})$	D_{3d}
Sb	2d	$(\frac{1}{3}, \frac{2}{3}, z), (\frac{2}{3}, \frac{1}{3}, -z)$	C_{3v}

In this section, we build an eight-band tight-binding (TB) model for CrSb and analyze the origin of the large spin splitting along the $\Gamma - M$ direction. As plotted in Fig. S1, from ab initio calculations, we find that the band structures near the Fermi level (E_F) are dominated by the d_{xz} , d_{yz} , $d_{x^2-y^2}$, and d_{xy} orbitals on Cr atoms. In Table 2, we tabulate the occupied Wyckoff positions (in space group $P\bar{3}m1$) for the spin-up Hamiltonian of CrSb, where the site symmetry of Cr is D_{3d} . For point group D_{3d} , both the orbitals (d_{xz}, d_{yz}) and $(d_{xy}, d_{x^2-y^2})$ have the same symmetry properties, corresponding to a two-fold irreducible presentation (irrep) E_g . Without loss of generality, we use the two orbitals ϕ_1 and ϕ_2 as the basis of irrep E_g to construct the tight-binding Hamiltonian. Note that the representation matrices of $(d_{xy}, d_{x^2-y^2})$ are the same with those of (d_{xz}, d_{yz}) under point group D_{3d} . Specifically, the creation operators of the spin-up atomic orbitals read

$$\hat{c}_{\mathbf{R}, Cr_1, \phi_1, \uparrow}^\dagger, \hat{c}_{\mathbf{R}, Cr_1, \phi_2, \uparrow}^\dagger, \hat{c}_{\mathbf{R}, Cr_2, \phi_1, \uparrow}^\dagger, \hat{c}_{\mathbf{R}, Cr_2, \phi_2, \uparrow}^\dagger, \quad (4)$$

where \mathbf{R} is the lattice vector. Here Cr₁ and Cr₂ denotes two Cr atoms with different Wyckoff positions (see Table 2). The four spin-down creation operators can be obtained by the spin group

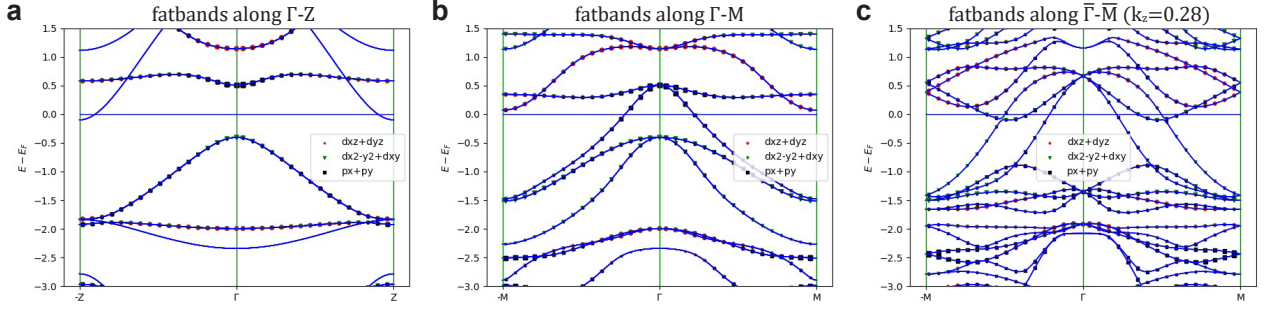


Fig. S1: The orbital-resolved magnetic band structures along **a** $\Gamma - Z$ ($k_1 = 0$ and $k_2 = 0$), **b** $\Gamma - M$ ($k_z = 0$), and **c** $\bar{\Gamma} - \bar{M}$ ($k_z = 0.28$). Here k_1, k_2 and k_z (or k_3) are along the direction of reciprocal lattice vectors. All the band structures are calculated without SOC. The weights of d_{xz} and d_{yz} orbitals on Cr, $d_{x^2-y^2}$ and d_{xy} orbitals on Cr, and p_x and p_y orbitals on Sb are plotted with red circles, green triangles, and black squares, respectively.

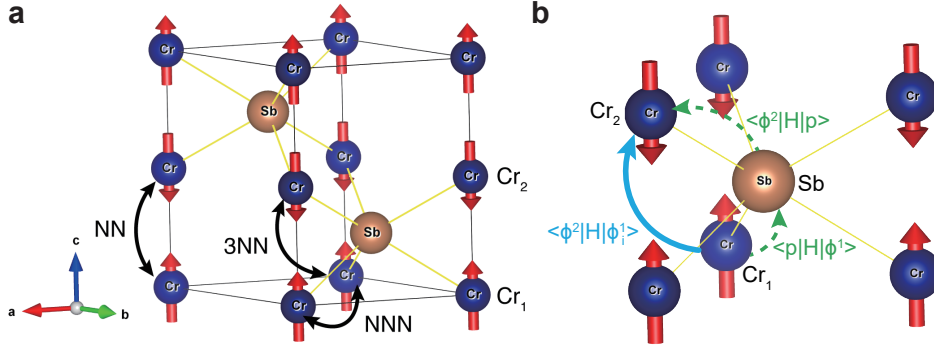


Fig. S2: **a** Chemical bonds between Cr and Sb atoms. The NN, NNN, and 3NN Cr-Cr bonds are indicated by the black arrow lines. **b** The dominant assistant hopping process between the 3NN Cr atoms at $(0, 0, 0)$ and $(1, 1, \frac{1}{2})$, which is mediated by the Sb at $(\frac{1}{3}, \frac{2}{3}, \frac{1}{4})$.

symmetry $\hat{P} = [C_2^s | \{M_z | (0, 0, \frac{1}{2})\}]$,

$$\begin{aligned}
 \hat{P} \hat{c}_{\mathbf{R}, Cr_1, \phi_1, \uparrow}^\dagger &= -\hat{c}_{\mathbf{R}, Cr_2, \phi_1, \downarrow}^\dagger \\
 \hat{P} \hat{c}_{\mathbf{R}, Cr_1, \phi_2, \uparrow}^\dagger &= -\hat{c}_{\mathbf{R}, Cr_2, \phi_2, \downarrow}^\dagger \\
 \hat{P} \hat{c}_{\mathbf{R}, Cr_2, \phi_1, \uparrow}^\dagger &= -\hat{c}_{\mathbf{R}, Cr_1, \phi_1, \downarrow}^\dagger \\
 \hat{P} \hat{c}_{\mathbf{R}, Cr_2, \phi_2, \uparrow}^\dagger &= -\hat{c}_{\mathbf{R}, Cr_1, \phi_2, \downarrow}^\dagger
 \end{aligned} \tag{5}$$

Then, the 8-band Hamiltonian is

$$H = \sum_{\mathbf{R}, \mathbf{R}', \tau, \tau', \alpha, \beta, s} \hat{c}_{\mathbf{R}+\tau, \alpha, s}^\dagger t_{\mathbf{R}+\tau, \mathbf{R}'+\tau'}^{\alpha s, \beta s} \hat{c}_{\mathbf{R}'+\tau', \beta, s} \tag{6}$$

where τ (τ') is the atom index representing Cr_1 or Cr_2 , α (β) is the orbital index, and s is the spin index.

As we have ignored the spin-orbit coupling in Eq. 6, the Hamiltonian in reciprocal space takes the following form,

$$H(\mathbf{k}) = \begin{bmatrix} H^\uparrow(\mathbf{k}) & 0_{4 \times 4} \\ 0_{4 \times 4} & H^\downarrow(\mathbf{k}) \end{bmatrix} = \sum_{i=0,3} \sum_{j,m=0,1,2,3} f_{ijm}(\mathbf{k}) \Gamma_{ijm} \tag{7}$$

where $\Gamma_{ijm} = s_i \otimes \sigma_j \otimes \tau_m \equiv s_i \sigma_j \tau_m$. The Pauli matrices $s_{i=0,1,2,3}$ (or σ_i or τ_i) represent the space of spin (or the two Cr sites or the two ϕ orbitals).

Let us consider the nearest neighbor (NN), the next nearest neighbor (NNN), and the third nearest neighbor (3NN) kinetic terms. As shown in Fig. S2a, the NN and 3NN bonds connect the two sublattices of Cr₁ and Cr₂, and the NNN bonds connect the Cr atoms within the same sublattice. There are two NN bonds for each Cr site, corresponding to $\mathbf{d} = \mathbf{R} + \tau - \mathbf{R}' - \tau' = (0, 0, \pm\frac{1}{2})$. Each Cr site has six NNN bonds, corresponding to the lattice vectors $\mathbf{d} = (1, 1, 0), (1, 0, 0), (0, 1, 0), (0, -1, 0), (-1, 0, 0), (-1, -1, 0)$. For each Cr site, there are 12 3NN bonds, corresponding to $\mathbf{d} = (1, 1, \frac{1}{2}), (1, 1, -\frac{1}{2}), (1, 0, \frac{1}{2}), (1, 0, -\frac{1}{2}), (0, 1, \frac{1}{2}), (0, 1, -\frac{1}{2}), (0, -1, \frac{1}{2}), (0, -1, -\frac{1}{2}), (-1, 0, \frac{1}{2}), (-1, 0, -\frac{1}{2}), (-1, -1, \frac{1}{2}), (-1, -1, -\frac{1}{2})$. Under this approximation, we perform Fourier transformation on the Hamiltonian in Eq. 6, and derive the Hamiltonian along $\Gamma - M$ direction as follows:

$$\begin{aligned}
H(\mathbf{k}) &= H_{on-site} + H_{NN} + H_{NNN} + H_{3NN} \\
&= H(\mathbf{r}) + \sum_{\mathbf{R} \in NN} e^{i\mathbf{k} \cdot \mathbf{R}} H(\mathbf{r} - \mathbf{R}) + \sum_{\mathbf{R} \in NNN} e^{i\mathbf{k} \cdot \mathbf{R}} H(\mathbf{r} - \mathbf{R}) + \sum_{\mathbf{R} \in 3NN} e^{i\mathbf{k} \cdot \mathbf{R}} H(\mathbf{r} - \mathbf{R}) \\
&= f_{000}(\mathbf{k})\Gamma_{000} + f_{001}(\mathbf{k})\Gamma_{001} + f_{003}(\mathbf{k})\Gamma_{003} + f_{010}(\mathbf{k})\Gamma_{010} + \\
&f_{011}(\mathbf{k})\Gamma_{011} + f_{013}(\mathbf{k})\Gamma_{013} + f_{330}(\mathbf{k})\Gamma_{330} + f_{331}(\mathbf{k})\Gamma_{331} + \\
&f_{333}(\mathbf{k})\Gamma_{333} + f_{311}(\mathbf{k})\Gamma_{311} + f_{313}(\mathbf{k})\Gamma_{313}
\end{aligned} \tag{8}$$

Here, we derive as follows the coefficients $f_{ijk}(\mathbf{k})$ along the $\Gamma - M$ ($\mathbf{k} = (k_1, 0, k_3)$) direction,

$$\begin{aligned}
f_{000}(\mathbf{k}) &= \frac{1}{2}(e_1 + e_2) - \frac{1}{3} \left(\sqrt{3}r_1 - 3r_2 - \sqrt{3}r_3 - 3r_4 \right) [2 \cos(k_1) + 1] \\
f_{001}(\mathbf{k}) &= (r_1 - r_3)[\cos(k_1) - 1] \\
f_{003}(\mathbf{k}) &= \frac{(r_1 - r_3)[\cos(k_1) - 1]}{\sqrt{3}} \\
f_{010}(\mathbf{k}) &= 2[2(q_1 + q_4) \cos(k_1) + q_1 + q_4 + t_1] \cos\left(\frac{k_3}{2}\right) \\
f_{011}(\mathbf{k}) &= 2\sqrt{3}(q_4 - q_1) \sin^2\left(\frac{k_1}{2}\right) \cos\left(\frac{k_3}{2}\right) \\
f_{013}(\mathbf{k}) &= 2(q_4 - q_1) \sin^2\left(\frac{k_1}{2}\right) \cos\left(\frac{k_3}{2}\right) \\
f_{330}(\mathbf{k}) &= \frac{1}{2}(e_1 - e_2) - \frac{1}{3} \left(\sqrt{3}r_1 - 3r_2 + \sqrt{3}r_3 + 3r_4 \right) [2 \cos(k_1) + 1] \\
f_{331}(\mathbf{k}) &= (r_1 + r_3)[\cos(k_1) - 1] \\
f_{333}(\mathbf{k}) &= \frac{(r_1 + r_3)[\cos(k_1) - 1]}{\sqrt{3}} \\
f_{311}(\mathbf{k}) &= 3(q_2 + q_3) \sin(k_1) \sin\left(\frac{k_3}{2}\right) \\
f_{313}(\mathbf{k}) &= \sqrt{3}(q_2 + q_3) \sin(k_1) \sin\left(\frac{k_3}{2}\right)
\end{aligned} \tag{9}$$

The free parameters in Eq. 9 are defined as follows:

- e_i ($i = 1, 2$) is the onsite energy of the orbitals ϕ_1 and ϕ_2 on Cr _{i} .
- t_1 is the kinetic hopping strength between two ϕ_1 (or the equivalent ϕ_2) orbitals on two NN Cr atoms.

- $r_i (i = 1, 2, 3, 4)$ is the kinetic hopping between two NNN Cr atoms, whose respective coordinates are $R_1 = (0, 0, 0)$ and $R_2 = (1, 1, 0)$. Specifically, $r_1 = \langle \phi_1, Cr_1, R_1 | \hat{H} | \phi_2, Cr_1, R_2 \rangle$, $r_2 = \langle \phi_1, Cr_1, R_1 | \hat{H} | \phi_1, Cr_1, R_2 \rangle$, $r_3 = \langle \phi_2, Cr_2, R_1 | \hat{H} | \phi_1, Cr_2, R_2 \rangle$, $r_4 = \langle \phi_2, Cr_2, R_1 | \hat{H} | \phi_2, Cr_2, R_2 \rangle$.
- $q_i (i=1,2,3,4)$ is the 3NN kinetic hopping from $R_1 = (0, 0, 0)$ to $R_2 = (1, 1, \frac{1}{2})$, defined as $q_1 = \langle \phi_1, Cr_1, R_1 | \hat{H} | \phi_1, Cr_2, R_2 \rangle$, $q_2 = \langle \phi_1, Cr_1, R_1 | \hat{H} | \phi_2, Cr_2, R_2 \rangle$, $q_3 = \langle \phi_2, Cr_1, R_1 | \hat{H} | \phi_1, Cr_2, R_2 \rangle$, $q_4 = \langle \phi_2, Cr_1, R_1 | \hat{H} | \phi_2, Cr_2, R_2 \rangle$.

To have an altermagnetic spin splitting (and band splitting), both the space-time reversal symmetry $[T||P]$ and the translational spin-rotation symmetry $[C_2^s||\vec{t}]$ (\vec{t} is a fractional lattice vector) are necessarily broken in the analytic Hamiltonian in Eq. 8. As mentioned in the main text, either of the above two symmetries guarantees a spin-degenerate band structure. In Eqs. 10-11, $[T||P]$ and $[C_2^s||\vec{t}]$ are defined using the orbital basis in Eqs. 4-5. We find that the first nine terms in Eq. 8 commute with the symmetry $[C_2^s||\vec{t}]$ and they do not give rise to the spin splitting along $\Gamma - M$ direction. In contrast, the last two terms, i.e. $f_{311}(\mathbf{k})\Gamma_{311}$ and $f_{313}(\mathbf{k})\Gamma_{313}$ which are proportional to $q_2 + q_3$, break both of the two spin group symmetries. Therefore the Hamiltonian in Eq. 8 has a finite spin splitting along $\Gamma - M$ direction when the 3NN hopping strength $q_2 + q_3$ is non-zero.

$$[T||P] = \begin{bmatrix} 0 & 0 & 0 & 0 & 1 & 0 & 0 & 0 \\ 0 & 0 & 0 & 0 & 0 & 1 & 0 & 0 \\ 0 & 0 & 0 & 0 & 0 & 0 & 1 & 0 \\ 0 & 0 & 0 & 0 & 0 & 0 & 0 & 1 \\ 1 & 0 & 0 & 0 & 0 & 0 & 0 & 0 \\ 0 & 1 & 0 & 0 & 0 & 0 & 0 & 0 \\ 0 & 0 & 1 & 0 & 0 & 0 & 0 & 0 \\ 0 & 0 & 0 & 1 & 0 & 0 & 0 & 0 \end{bmatrix} K = s_1\sigma_0\tau_0K, \text{ where } K \text{ is complex conjugate operator.} \quad (10)$$

$$[C_2^s||\vec{t} = (0, 0, 1/2)] = \begin{bmatrix} 0 & 0 & 0 & 0 & 0 & 0 & 1 & 0 \\ 0 & 0 & 0 & 0 & 0 & 0 & 0 & 1 \\ 0 & 0 & 0 & 0 & 1 & 0 & 0 & 0 \\ 0 & 0 & 0 & 0 & 0 & 1 & 0 & 0 \\ 0 & 0 & 1 & 0 & 0 & 0 & 0 & 0 \\ 0 & 0 & 0 & 1 & 0 & 0 & 0 & 0 \\ 1 & 0 & 0 & 0 & 0 & 0 & 0 & 0 \\ 0 & 1 & 0 & 0 & 0 & 0 & 0 & 0 \end{bmatrix} = s_1\sigma_1\tau_0 \quad (11)$$

By fitting the band structure from ab initio calculations, especially the dispersion along $\Gamma - M$ direction near the Fermi level, we obtain the parameters in Eq. 9, as tabulated in Table 3. The comparison between band structures from ab initio calculation and the tight-binding model is plotted in Fig. S3.

Table 3: Parameters in the TB model (Eq. 9) obtained by fitting to the ab initio calculation. The unit is eV.

e_1	e_2	t_1	r_1	r_2	r_3	r_4	q_1	$q_2 + q_3$	q_4
-3.5883	-1.4522	1.6	-0.1	0.305	0.1	-0.12	-0.0184	0.195	0.1942

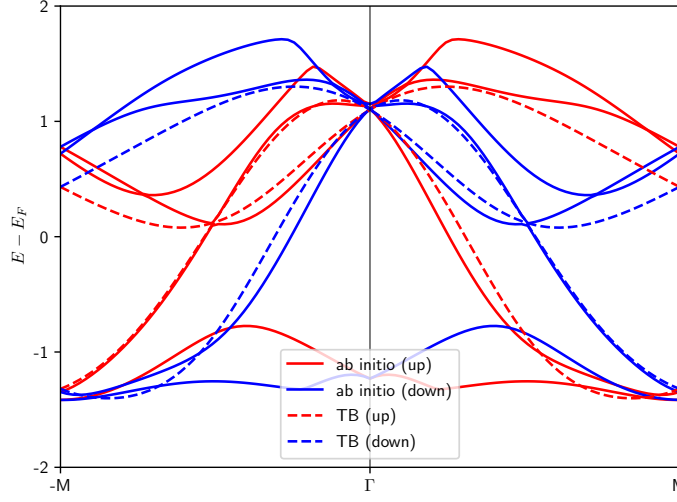


Fig. S3: Band structures along $\Gamma - M$ direction at $k_z = 0.28$. The solid (dashed) lines represent the band dispersion obtained from ab initio calculation (TB model). The red and blue colors represent spin-up and spin-down band sets, respectively.

2 Derivation of the 3NN hopping parameters

In the above section, we have analyzed qualitatively the origin of the spin/band splitting along $\Gamma - M$ direction, which is proportional to the kinetic hopping between the two d orbitals on the two 3NN Cr atoms. Usually, the Wannier functions of d orbitals are very local, and the hopping between them is tiny. While in Table 3, the fitted 3NN hopping is in the same order as the NNN hopping, which is counterintuitive. To have a deep understanding of this, it is necessary to derive the 3NN hopping parameters from ab initio calculations.

Based on the Wannier calculations, we find that the bands near E_F come from a strong hybridization between the two E_g orbitals (d_{xz}, d_{yz}) and ($d_{xy}, d_{x^2-y^2}$), and they can be characterized approximately by a set of hybridized orbitals, defined as follows,

$$\begin{aligned}
 |\phi_1^1, Cr_1\rangle &= \frac{\sqrt{2}}{2}(-|d_{xz}, Cr_1\rangle - |d_{xy}, Cr_1\rangle) \\
 |\phi_2^1, Cr_1\rangle &= \frac{\sqrt{2}}{2}(|d_{yz}, Cr_1\rangle + |d_{x^2-y^2}, Cr_1\rangle) \\
 |\phi_1^2, Cr_1\rangle &= \frac{\sqrt{2}}{2}(-|d_{xz}, Cr_1\rangle + |d_{xy}, Cr_1\rangle) \\
 |\phi_2^2, Cr_1\rangle &= \frac{\sqrt{2}}{2}(-|d_{yz}, Cr_1\rangle + |d_{x^2-y^2}, Cr_1\rangle) \\
 |\phi_1^1, Cr_2\rangle &= \frac{\sqrt{2}}{2}(|d_{xz}, Cr_2\rangle - |d_{xy}, Cr_2\rangle) \\
 |\phi_2^1, Cr_2\rangle &= \frac{\sqrt{2}}{2}(|d_{yz}, Cr_2\rangle - |d_{x^2-y^2}, Cr_2\rangle) \\
 |\phi_1^2, Cr_2\rangle &= \frac{\sqrt{2}}{2}(|d_{xz}, Cr_2\rangle + |d_{xy}, Cr_2\rangle) \\
 |\phi_2^2, Cr_2\rangle &= \frac{\sqrt{2}}{2}(|d_{yz}, Cr_2\rangle + |d_{x^2-y^2}, Cr_2\rangle)
 \end{aligned} \tag{12}$$

where $|\phi_i^j, Cr_\alpha\rangle$ is the i^{th} orbital basis of the j^{th} hybridized E_g orbital on Cr_α . Using the orbital transformation in Eq. 12, we replot the orbital resolved band structures in Fig. S4. It shows that the bands crossing E_F are mainly contributed by the second E_g orbital on Cr_1 (consisting of $|\phi_1^2, Cr_1\rangle$ and $|\phi_2^2, Cr_1\rangle$) and the first E_g orbital on Cr_2 (consisting of $|\phi_1^1, Cr_2\rangle$ and $|\phi_2^1, Cr_2\rangle$). As obtained from the Wannier calculations (see Table 5 below), the direct 3NN hopping between them (i.e. $q_2 + q_3$ in Eq. 9) is about 21 meV, which is much smaller than the fitted value 173 meV. We also notice that the Wannier functions of p orbitals on Sb have a large spread and they hybridize significantly with the local d orbitals. Hence the large value of $q_2 + q_3$ should be dominated by a second-order hopping process mediated by Sb, or in other words, the p orbitals on Sb assist the 3NN hopping between d orbitals on Cr.

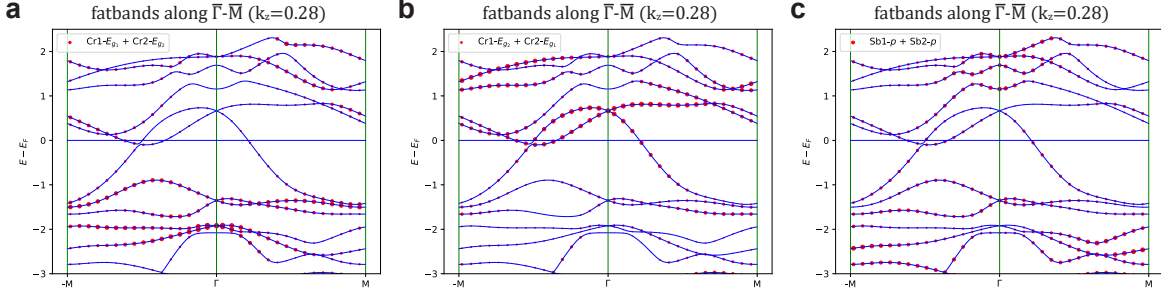


Fig. S4: The orbital-resolved band structures of the spin up component along $\Gamma - M$ direction at $k_z = 0.28$. The orbital weights of **a** $|\phi_1^2, Cr_2\rangle, |\phi_2^2, Cr_2\rangle, |\phi_1^1, Cr_1\rangle$ and $|\phi_2^1, Cr_1\rangle$ **b** $|\phi_1^2, Cr_1\rangle, |\phi_2^2, Cr_1\rangle, |\phi_1^1, Cr_2\rangle$ and $|\phi_2^1, Cr_2\rangle$, **c** $|p_z\rangle, |p_x\rangle$ and $|p_y\rangle$ on Sb, are plotted with red circles.

The assistant hopping between d orbitals from \mathbf{r}_i to \mathbf{r}_j and mediated by the p orbitals at \mathbf{r}_k can be calculated in the second-order approximation,

$$\tilde{t}_{ij} \approx \frac{t_{ik}t_{kj}}{(\Delta_i - \Delta_k)(\Delta_k - \Delta_j)} \quad (13)$$

where t_{ik} is the direct hopping between d orbital at \mathbf{r}_i and p orbital at \mathbf{r}_k , and $\Delta_{i,j,k}$ is the onsite energy of the corresponding orbital at $\mathbf{r}_{i,j,k}$. Using the second-order perturbation, we have calculated all the possible assistant hopping process between the d orbitals on Cr_1 at site $(0, 0, 0)$ and the d orbitals on Cr_2 at site $(1, 1, \frac{1}{2})$, and tabulated the ones contributing an assistant hopping larger than 10 meV in Table 4. It shows that the assistant hopping process mediated by the Sb at site $(\frac{1}{3}, \frac{2}{3}, \frac{1}{4})$, as schematically shown in Fig. S2b, is much more significant than the others. Indeed, it is the shortest path between the 3NN Cr atoms. By summing the direct hopping and all the assistant hopping obtained from the second-order perturbation, we derive the effective hopping values for q_1 , $q_2 + q_3$, and q_4 , as tabulated in Table 5. All of the values are approximately equal to the fitted parameters in Table 3.

Table 4: All the second-order processes that contribute an assistant hopping larger than 10 meV. The energy unit is eV.

second order process	t_{ik}	t_{kj}	Δ_i	Δ_k	Δ_j	\tilde{t}_{ij}
$\text{Cr}[0,0,0] \phi_1^2\rangle \rightarrow \text{Sb}[-2/3,-1/3,1/4] \text{px} \rightarrow \text{Cr}[1,1,1/2] \phi_1^1\rangle$	-0.7343	-0.0443	8.1243	7.1126	9.9428	-0.0114
$\text{Cr}[0,0,0] \phi_1^2\rangle \rightarrow \text{Sb}[-1/3,1/3,-1/4] \text{pz} \rightarrow \text{Cr}[1,1,1/2] \phi_1^1\rangle$	0.5125	0.0142	8.1243	7.8535	9.9428	-0.0128
$\text{Cr}[0,0,0] \phi_1^2\rangle \rightarrow \text{Sb}[1/3,-1/3,1/4] \text{px} \rightarrow \text{Cr}[1,1,1/2] \phi_1^1\rangle$	-0.7343	0.0825	8.1243	7.1126	9.9428	0.0212
$\text{Cr}[0,0,0] \phi_1^2\rangle \rightarrow \text{Sb}[4/3,2/3,1/4] \text{pz} \rightarrow \text{Cr}[1,1,1/2] \phi_1^1\rangle$	-0.0486	-0.2599	8.1243	7.8535	9.9428	-0.0223
$\text{Cr}[0,0,0] \phi_1^2\rangle \rightarrow \text{Sb}[1/3,-1/3,1/4] \text{pz} \rightarrow \text{Cr}[1,1,1/2] \phi_2^1\rangle$	-0.5125	0.0245	8.1243	7.8535	9.9422	0.0222
$\text{Cr}[0,0,0] \phi_1^2\rangle \rightarrow \text{Sb}[2/3,1/3,-1/4] \text{pz} \rightarrow \text{Cr}[1,1,1/2] \phi_2^1\rangle$	-0.5125	0.0263	8.1243	7.8535	9.9422	0.0238
$\text{Cr}[0,0,0] \phi_1^2\rangle \rightarrow \text{Sb}[2/3,1/3,3/4] \text{pz} \rightarrow \text{Cr}[1,1,1/2] \phi_2^1\rangle$	0.0758	0.3003	8.1243	7.8535	9.9422	-0.0403
$\text{Cr}[0,0,0] \phi_1^2\rangle \rightarrow \text{Sb}[4/3,2/3,1/4] \text{pz} \rightarrow \text{Cr}[1,1,1/2] \phi_2^1\rangle$	-0.0486	0.1502	8.1243	7.8535	9.9422	0.0129
$\text{Cr}[0,0,0] \phi_2^2\rangle \rightarrow \text{Sb}[-1/3,-2/3,-1/4] \text{pz} \rightarrow \text{Cr}[1,1,1/2] \phi_1^1\rangle$	0.5915	0.0184	8.1231	7.8535	9.9428	-0.0193
$\text{Cr}[0,0,0] \phi_2^2\rangle \rightarrow \text{Sb}[1/3,-1/3,1/4] \text{px} \rightarrow \text{Cr}[1,1,1/2] \phi_1^1\rangle$	0.4282	0.0825	8.1231	7.1126	9.9428	-0.0124
$\text{Cr}[0,0,0] \phi_2^2\rangle \rightarrow \text{Sb}[1/3,2/3,1/4] \text{pz} \rightarrow \text{Cr}[1,1,1/2] \phi_1^1\rangle$	-0.5915	0.2599	8.1231	7.8535	9.9428	0.2728
$\text{Cr}[0,0,0] \phi_2^2\rangle \rightarrow \text{Sb}[1/3,2/3,1/4] \text{py} \rightarrow \text{Cr}[1,1,1/2] \phi_1^1\rangle$	-0.9812	-0.3392	8.1231	7.1119	9.9428	-0.1162
$\text{Cr}[0,0,0] \phi_2^2\rangle \rightarrow \text{Sb}[2/3,4/3,3/4] \text{pz} \rightarrow \text{Cr}[1,1,1/2] \phi_1^1\rangle$	-0.0369	0.2599	8.1231	7.8535	9.9428	0.017
$\text{Cr}[0,0,0] \phi_2^2\rangle \rightarrow \text{Sb}[4/3,2/3,1/4] \text{pz} \rightarrow \text{Cr}[1,1,1/2] \phi_1^1\rangle$	-0.0282	-0.2599	8.1231	7.8535	9.9428	-0.013
$\text{Cr}[0,0,0] \phi_2^2\rangle \rightarrow \text{Sb}[1/3,-1/3,1/4] \text{pz} \rightarrow \text{Cr}[1,1,1/2] \phi_2^1\rangle$	0.2957	0.0245	8.1231	7.8535	9.9422	-0.0129
$\text{Cr}[0,0,0] \phi_2^2\rangle \rightarrow \text{Sb}[2/3,1/3,-1/4] \text{pz} \rightarrow \text{Cr}[1,1,1/2] \phi_2^1\rangle$	-0.2957	0.0263	8.1231	7.8535	9.9422	0.0138
$\text{Cr}[0,0,0] \phi_2^2\rangle \rightarrow \text{Sb}[1/3,2/3,1/4] \text{pz} \rightarrow \text{Cr}[1,1,1/2] \phi_2^1\rangle$	-0.5915	0.1502	8.1231	7.8535	9.9422	0.1577
$\text{Cr}[0,0,0] \phi_2^2\rangle \rightarrow \text{Sb}[1/3,2/3,1/4] \text{py} \rightarrow \text{Cr}[1,1,1/2] \phi_2^1\rangle$	-0.9812	0.2919	8.1231	7.1119	9.9422	0.1001
$\text{Cr}[0,0,0] \phi_2^2\rangle \rightarrow \text{Sb}[2/3,1/3,3/4] \text{pz} \rightarrow \text{Cr}[1,1,1/2] \phi_2^1\rangle$	0.0435	0.3003	8.1231	7.8535	9.9422	-0.0232

Table 5: The direct, assitant, and effective (total) hopping values of parameters $q_1, q_2 + q_3, q_4$. The energy unit is eV.

	q_1	$q_2 + q_3$	q_4
t_{direct}	0.005	0.0214	-0.066
\tilde{t}	-0.0234	0.1516	0.2602
$t_{eff} = t_{direct} + \tilde{t}$	-0.0184	0.1730	0.1942

3 Matrix representation of the crystalline symmetries

In this section, we provide the matrix representations of all the symmetries \hat{R} that leave the Hamiltonian \hat{H}_\uparrow in Eq. (6) invariant,

$$\hat{H}_\uparrow = \hat{R}^{-1} \hat{H}_\uparrow \hat{R} \quad (14)$$

We still use the atomic basis as defined in Eq. (4).

Identity operation \hat{E} :

$$\hat{E} = \begin{pmatrix} 1 & 0 & 0 & 0 \\ 0 & 1 & 0 & 0 \\ 0 & 0 & 1 & 0 \\ 0 & 0 & 0 & 1 \end{pmatrix}$$

The two three-fold rotation symmetry along the z -axis \hat{C}_{3z}^i :

$$\hat{C}_{3z}^1 = \begin{pmatrix} -\frac{1}{2} & -\frac{\sqrt{3}}{2} & 0 & 0 \\ \frac{\sqrt{3}}{2} & -\frac{1}{2} & 0 & 0 \\ 0 & 0 & -\frac{1}{2} & -\frac{\sqrt{3}}{2} \\ 0 & 0 & \frac{\sqrt{3}}{2} & -\frac{1}{2} \end{pmatrix}$$

$$\hat{C}_{3z}^2 = \begin{pmatrix} -\frac{1}{2} & \frac{\sqrt{3}}{2} & 0 & 0 \\ -\frac{\sqrt{3}}{2} & -\frac{1}{2} & 0 & 0 \\ 0 & 0 & -\frac{1}{2} & \frac{\sqrt{3}}{2} \\ 0 & 0 & \frac{\sqrt{3}}{2} & -\frac{1}{2} \end{pmatrix}$$

The two-fold rotation symmetry along the x -axis \hat{C}_{2x} :

$$\hat{C}_{2x} = \begin{pmatrix} -1 & 0 & 0 & 0 \\ 0 & 1 & 0 & 0 \\ 0 & 0 & -1 & 0 \\ 0 & 0 & 0 & 1 \end{pmatrix}$$

Inversion symmetry \hat{P} :

$$\hat{P} = \begin{pmatrix} 1 & 0 & 0 & 0 \\ 0 & 1 & 0 & 0 \\ 0 & 0 & 1 & 0 \\ 0 & 0 & 0 & 1 \end{pmatrix}$$

All the generators of unitary-operation \hat{R} are listed above. The anti-unitary operations satisfied by \hat{H}_\uparrow are $\hat{R}\hat{T}$, where \hat{T} is the time-reversal operation:

$$\hat{T} = \begin{pmatrix} 1 & 0 & 0 & 0 \\ 0 & 1 & 0 & 0 \\ 0 & 0 & 1 & 0 \\ 0 & 0 & 0 & 1 \end{pmatrix} \hat{K}$$

where \hat{K} is the complex conjugate operation: $\hat{K}c = c^*\hat{K}$, c is a complex number.

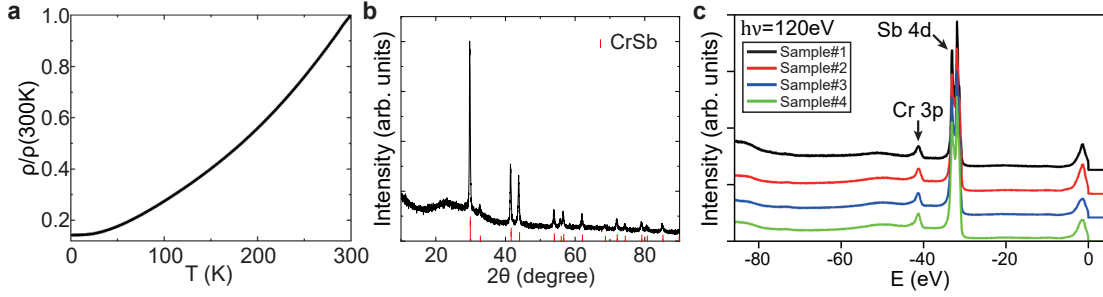


Fig. S5: Additional characterizations of CrSb. **a** Normalized resistivity ($\rho/\rho(300\text{ K})$) as a function of temperature for a typical CrSb single crystal. **b** Powder XRD pattern from a polycrystal CrSb sample (black curve). The expected peaks for CrSb are shown at the bottom. **c** Core level scans taken with 120 eV photons from four different samples, showing the Cr 3p and Sb 4d peaks without any trace of impurities. The strong Sb 4d peaks imply possibly Sb-terminated surface.

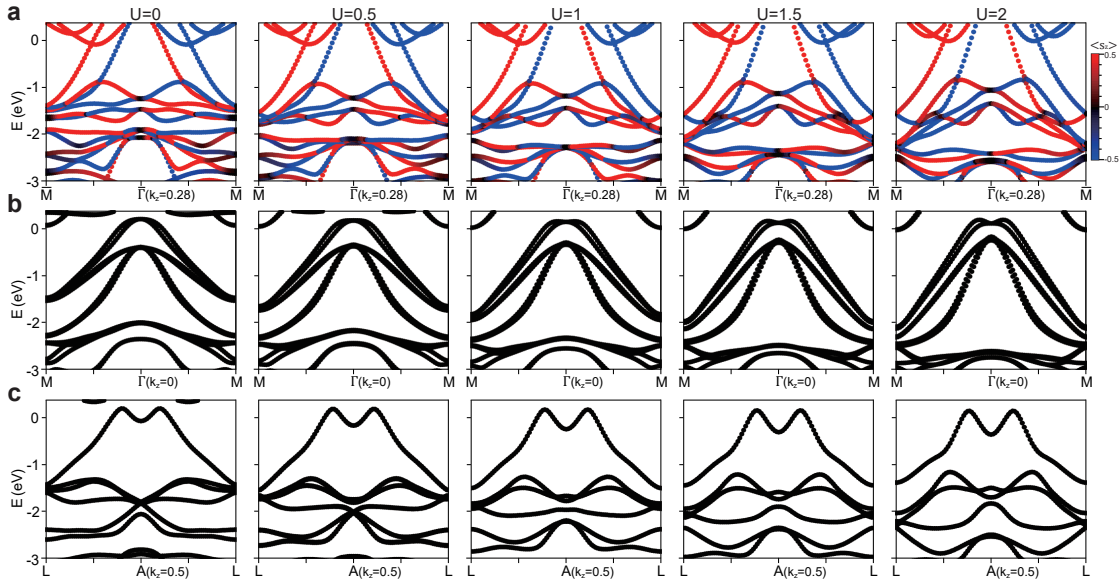


Fig. S6: Calculated band structure along $\bar{M} - \bar{\Gamma} - \bar{M}$ at $k_z = 0.28c^*$ (**a**), 0 (**b**) and $0.5c^*$ (**c**). From left to right: calculation results with the Coulomb repulsion U set to 0, 0.5, 1, 1.5 and 2 eV. Since the $U = 0$ eV calculation yields best agreement with ARPES data, we choose $U = 0$ eV for all the calculations in the paper.

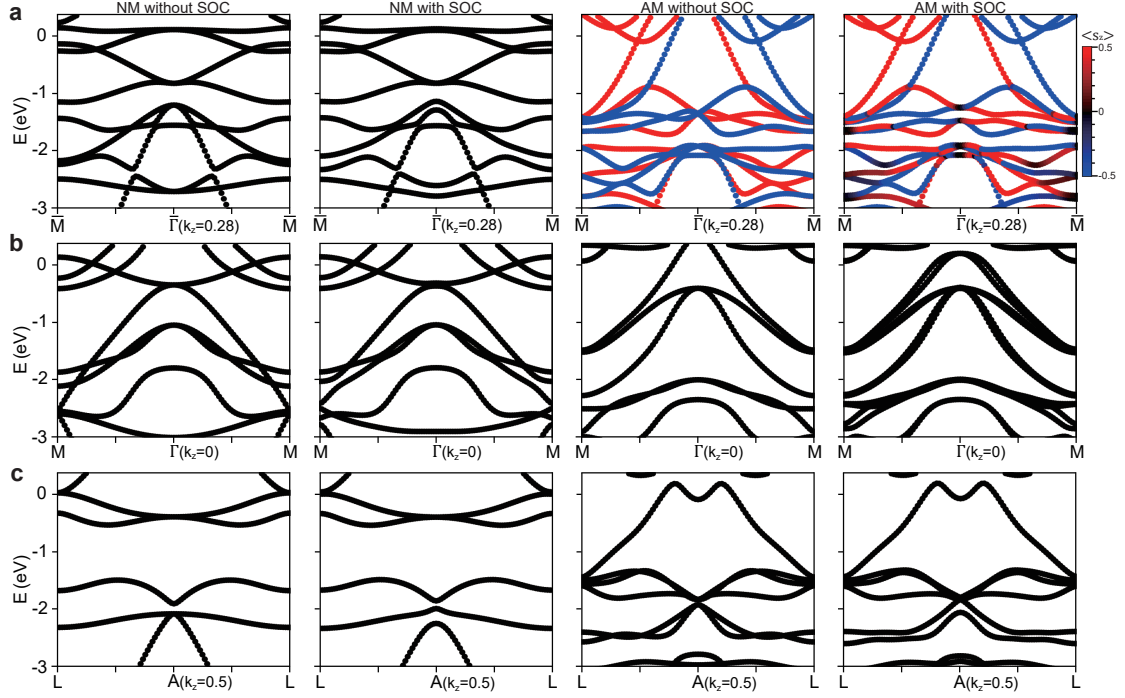


Fig. S7: Calculated band structure for CrSb at $k_z = 0.28c^*$ (a), 0 (b) and $0.5c^*$ (c). From left to right: calculation ignoring both altermagnetism and SOC [nonmagnetic (NM) without SOC], ignoring altermagnetism but considering SOC (NM with SOC), considering altermagnetism but ignoring SOC [altermagnetism (AM) without SOC], considering both altermagnetism and SOC [AM with SOC]. The colors of the curves indicate spin polarization (color bar on the right).

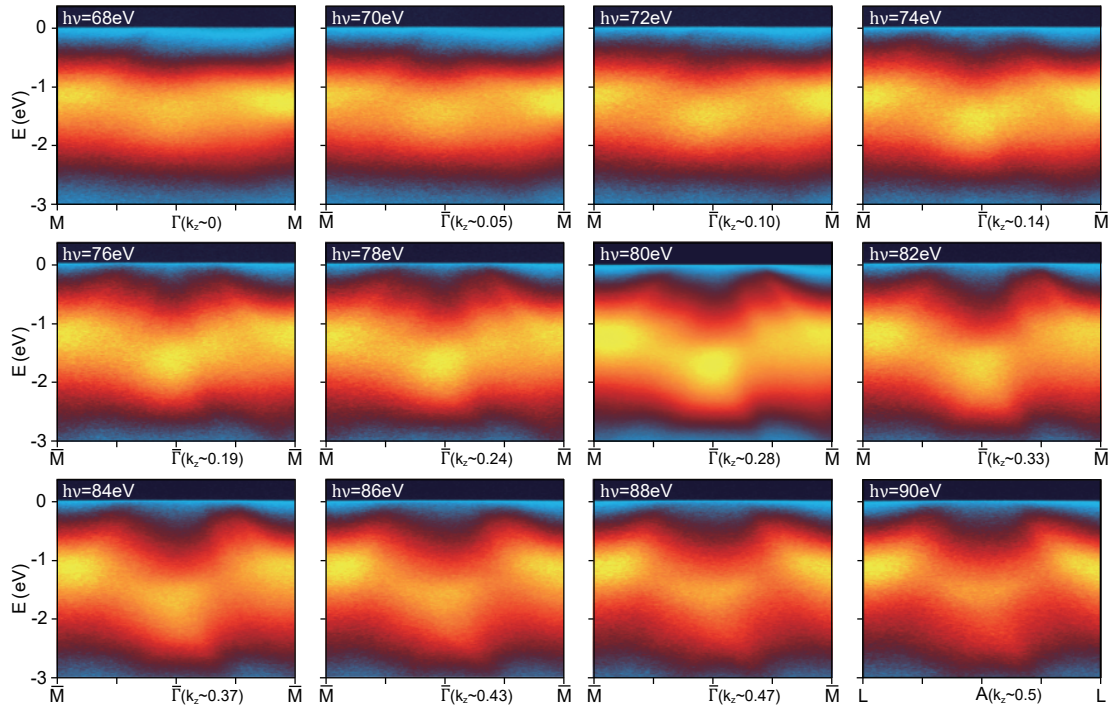


Fig. S8: The ARPES spectra along the $\bar{M} - \bar{\Gamma} - \bar{M}$ direction taken with different photon energies. The corresponding k_z values (in units of c^*) are also indicated.

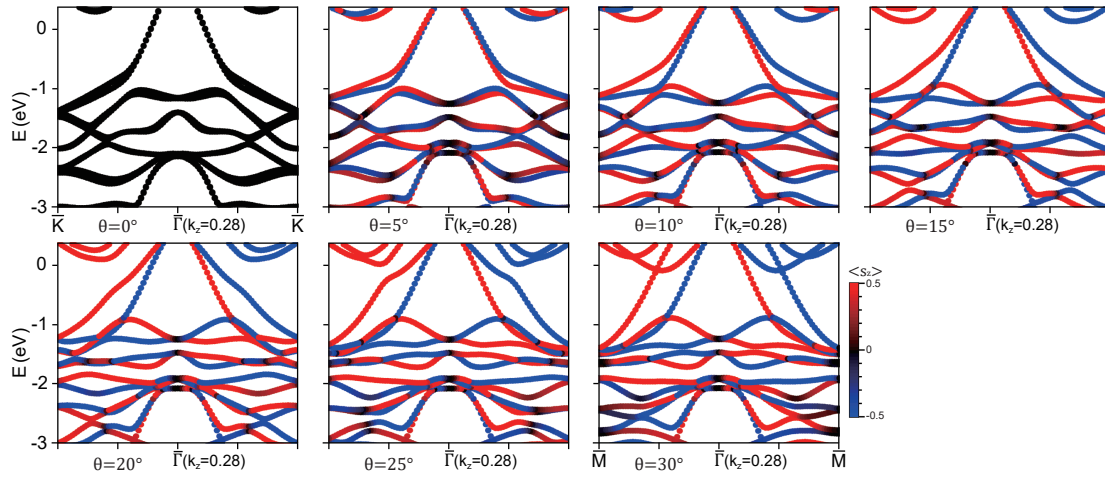


Fig. S9: Calculated in-plane band dispersion at $k_z \sim 0.28c^*$ for different θ angles (defined in Fig. 3a). The altermagnetic splitting shows a monotonic increase from $\bar{K} - \bar{\Gamma} - \bar{K}$ ($\theta = 0^\circ$) to $\bar{M} - \bar{\Gamma} - \bar{M}$ ($\theta = 30^\circ$).

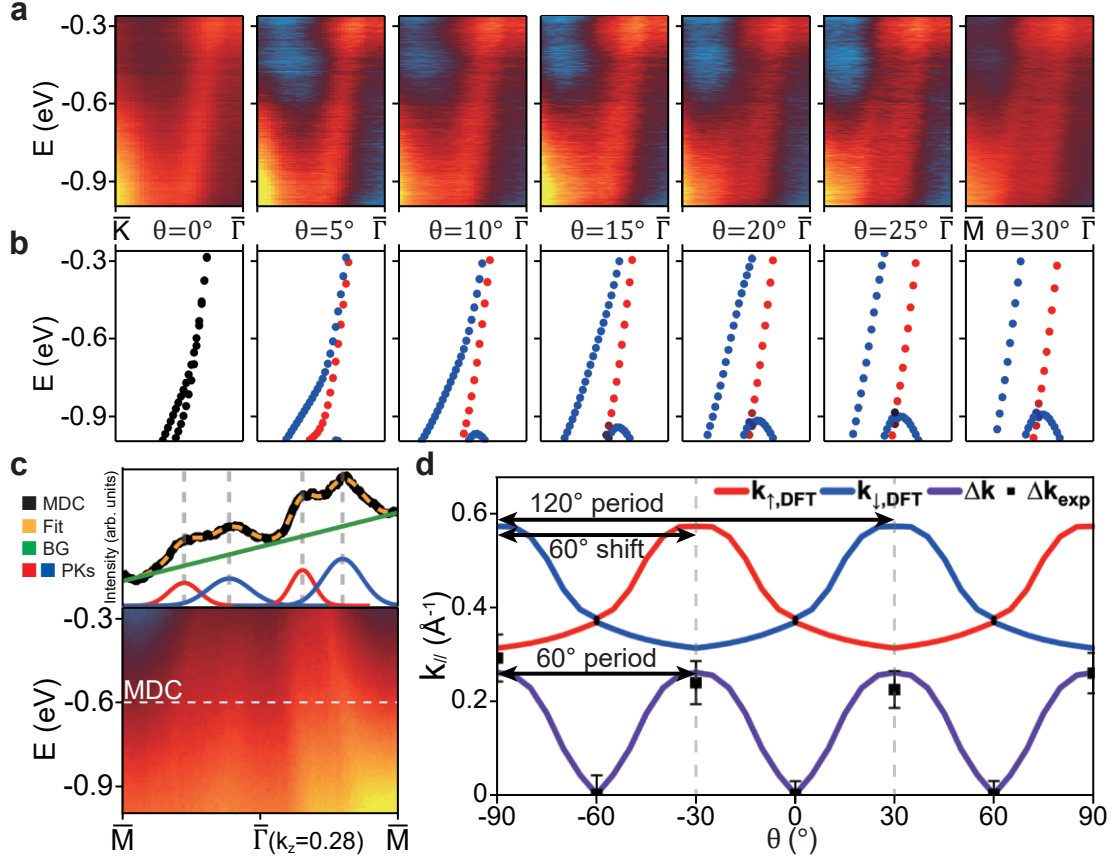


Fig. S10: Additional ARPES data and analysis illustrating the in-plane altermagnetic splitting. **a** Energy-momentum cuts for different θ angles with a small step of 5° , extracted from Fig. 3a. **b** Band structure from DFT for comparison with (a). **c** Illustration of peak fitting from the momentum distribution curve (MDC). A Gaussian shape is assumed for all the peaks and a smooth background is included. The raw data, fitting result (Fit), background (BG) and Gaussian peaks (PKs) are shown respectively. **d** The in-plane momentum of up-spin ($k_{\uparrow,DFT}$, red curve) and down-spin ($k_{\downarrow,DFT}$, blue curve) bands at $E = -0.6$ eV as a function of θ from DFT. The purple curve is the magnitude of spin splitting ($\Delta k = |k_{\uparrow,DFT} - k_{\downarrow,DFT}|$). The black boxes with error bars are experimental results at high-symmetry points.

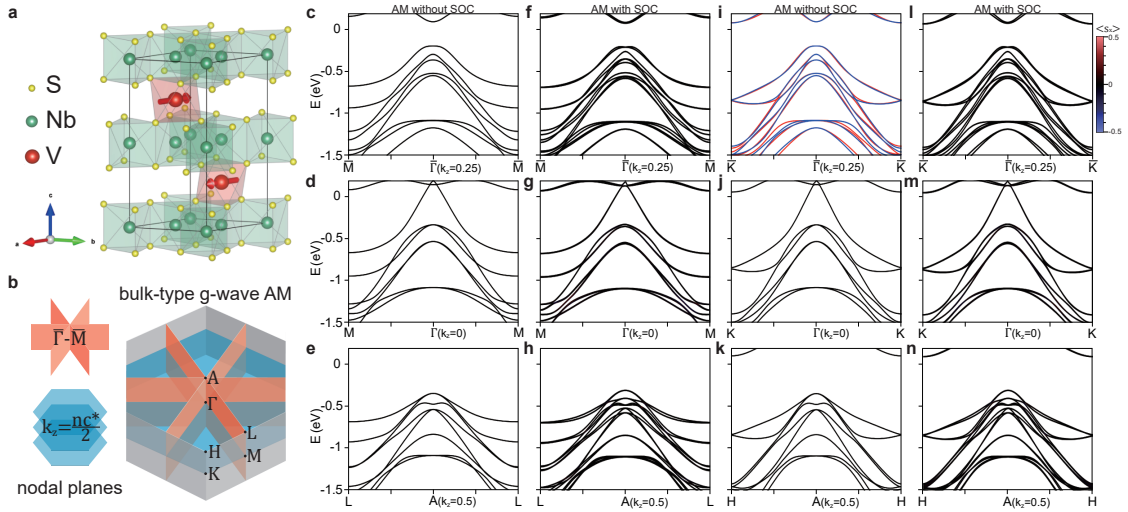


Fig. S11: Bulk-type g -wave altermagnet VNb_3S_6 with much smaller splitting than CrSb . **a** Spin and lattice structure of VNb_3S_6 . **b** The BZ with high symmetry points and nodal planes labelled. Three equivalent nodal planes parallel to k_z are along $\bar{M} - \bar{\Gamma} - \bar{M}$. **c-n** DFT calculations along $\bar{\Gamma} - \bar{M}$ (**c-h**) and $\bar{\Gamma} - \bar{K}$ (**i-n**) at $k_z = 0.25$ (top row), 0 (middle row), 0.5 (bottom row) c^* , respectively. Calculations with SOC (**f,g,h,l,m,n**) and without SOC (**c,d,e,i,j,k**) are both considered. SOC has only minor effect on the band dispersion, despite reducing the spin polarization. The magnitude of altermagnetic splitting is about a few tens of meV, much smaller than CrSb .

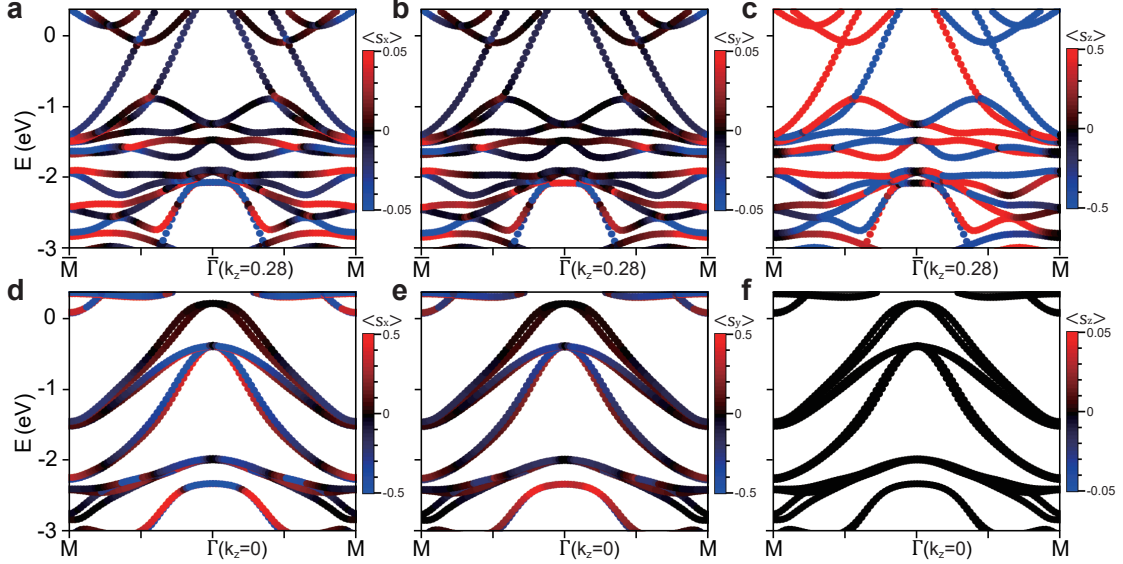


Fig. S12: Spin polarizations of DFT bands along x , y and z directions considering both altermagnetism and SOC. **a-c** Spin polarizations along x (**a**, $\langle S_x \rangle$), y (**b**, $\langle S_y \rangle$) and z (**c**, $\langle S_z \rangle$) directions, for bands along $\bar{\Gamma} - \bar{M}$ at $k_z = 0.28c^*$. Please note the much larger color scales (shown on the right) for (**c**) compared to (**a-b**). For bands away from E_F , i.e., $E \sim -2.5$ eV where appreciable contributions from Sb p orbitals are present, the inclusion of SOC makes $\langle S_z \rangle$ deviate from the quantized value of $\pm 1/2$, leading to small $\langle S_x \rangle$ and $\langle S_y \rangle$ components shown in (**a-b**). However, for bands near E_F , $\langle S_z \rangle$ is still close to $\pm 1/2$, indicating weak SOC effects. **d-f** Spin polarizations along x (**d**, $\langle S_x \rangle$), y (**e**, $\langle S_y \rangle$) and z (**f**, $\langle S_z \rangle$) directions, for bands along $\bar{\Gamma} - \bar{M}$ at $k_z = 0$. Without SOC, this k_z plane is a nodal plane without altermagnetic splitting. The inclusion of SOC induces a very tiny splitting (see also Fig. S7). While the spin polarization along the z direction remains zero (**f**), protected by $[C_2^S \parallel M_z]$, there is a very small in-plane spin polarization due to SOC (**d,e**). This is similar to the weak altermagnetic splitting discussed in [13].

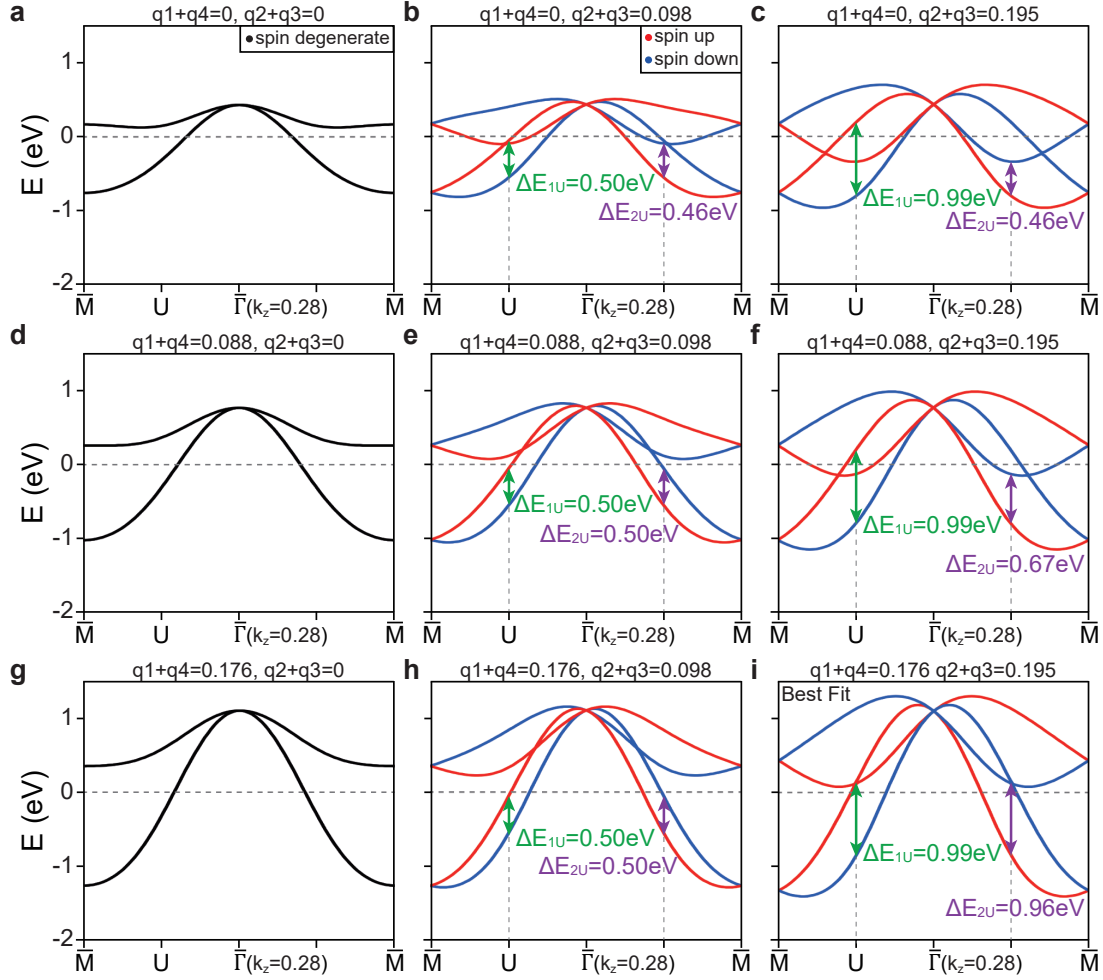


Fig. S13: Dependence of band dispersion on different 3NN hopping parameters. Band dispersions along the $\bar{\Gamma} - \bar{M}$ direction at $k_z = 0.28c^*$ are obtained from the eight-band TB model using different $q_1 + q_4$ and $q_2 + q_3$ values, as indicated at the top of each figure. The red, blue and black lines represent spin-up, spin-down and spin-degenerate bands, respectively.